Frequency domain Bernstein-Bézier finite element solver for modelling short waves in elastodynamics

N. Benatia[a], A. El Kacimi*[,a], O. Laghrouche[b], M. El Alaoui Talibi[c], and J. Trevelyan[d]

[a]LMC, Department of Mathematics and Computer Science, FPS, Cadi Ayyad University, Morocco
[b]Institute for Infrastructure and Environment, Heriot-Watt University, Edinburgh EH14 4AS, UK
[c]LIBMA, Department of Mathematics, FSSM, Cadi Ayyad University, Morocco
[d]Department of Engineering, Durham University, Durham DH1 3LE, UK

Abstract

This work presents a high-order Bernstein-Bézier finite element (FE) discretisation to accurately solve time harmonic elastic wave problems on unstructured triangular mesh grids. Although high-order FEs possess many advantages over standard FEs, the computational cost of matrix assembly is a major issue in high-order computations. A key ingredient to address this drawback is to resort to low complexity procedures in building the local high order FE matrices. This is achieved in this work by exploiting the tensorial property of Bernstein polynomials and applying the sum factorisation method for curved elements. An efficient implementation of the analytical rules for affine elements is also proposed. Furthermore, element-level static condensation of the interior degrees of freedom is performed to reduce the memory requirements. Additionally, the applicability of the method with a variable polynomial order, based on a simple a priori indicator, is investigated.

The computational complexities of sum factorisation, analytical rules and standard quadrature are first evaluated, in terms of the CPU time against the polynomial order. The analysis shows that the achieved numerical complexities compare favourably to those expected theoretically. A significant runtime saving is also obtained by using analytical rules and sum factorisation. The performance of the Bernstein-Bézier FEs is then assessed on various benchmark tests, over a wide range of frequencies. Results from the elastic wave scattering problem demonstrate the effectiveness of this method in coping with the pollution error, and its accuracy in resolving high order evanescent wave modes. Additionally, a wave transmission problem with high wave speeds contrast and a curved interior interface is considered, where a simple *a priori* indicator is proposed to assign the variable polynomial order. The study provides evidence of the great benefit of a non uniform p-refinement in reducing the computational cost and enhancing accuracy.

Keywords. Finite elements; Bernstein-Bézier; Numerical integration; Sum factorisation; Static condensation; Short wave Scattering; Linear elasticity.

1 Introduction

Computer modelling of elastic wave propagation and scattering is an effective tool for predicting and testing in a wide variety of practical applications, including traffic-induced vibrations from roads and railways, seismic induced vibrations, seismic inversion, design of foundation elements, geophysical exploration, nondestructive evaluation and structural engineering.

The Finite Element Method (FEM) is a popular discretisation method commonly adopted for the numerical solution of wave problems. It is favoured over other methods, owing to its ability in accurately handling complex geometries, material heterogeneity and anisotropy. When typically piecewise linear FEs are used, around ten grid points per wavelength are needed to ensure a satisfactory

*Corresponding author: abdellah.elkacimi@uca.ma

resolution of the wave pattern. It is noteworthy that this rule of thumbnail of ten nodal points per wavelength enables to control the local approximation error [1]. However, due to the pollution effect in the mid or high frequency regimes [1–4], even more than ten nodal points are required to achieve an acceptable level of accuracy, and thus the procedure becomes prohibitively expensive and less effective.

The past few decades have seen many attempts to design robust numerical schemes alleviating the pollution phenomenon. A substantial improvement was made in developing wave based, or Trefftz, methods enabling to achieve engineering accuracy with a significant reduction in the computational effort. The common idea in these approaches is to incorporate the oscillatory behaviour of the solution into the approximate space by including plane waves or Bessel functions. Examples of such methods, among others, are the Partition of Unity Finite Element Method (PUFEM) [5–14], the Generalized Finite Element Method (GFEM) [15, 16], the Ultra Weak Variational Formulation (UWVF) [17–19], the least-squares method [20], the Discontinuous Enrichment Method (DEM) [21, 22] and the wave-based discontinuous Galerkin method [23–25]. It is worth noticing that all the aforementioned methods (except PUFEM, GFEM and DEM) share the same discontinuous Galerkin framework and differ only in the used numerical fluxes to ensure continuity between elements [26].

Wave based methods generally make use of the plane wave basis decomposition by pressure and shear waves in the approximation of time harmonic elastic wave problems. Perrey-Debain *et al.* [27] proposed the partition of unity boundary element method. Huttunen *et al.* [28, 29] developed the UWVF in two and three space dimensions. Also, Zhang *et al.* [30] extended the DEM to frequency domain elastic wave computations. Note that inter-element continuity in the UWVF and DEM is, respectively, enforced weakly by means of numerical fluxes and Lagrange multipliers. In References [31–35] and [36], PUFEM was successfully applied to time harmonic elastic wave problems, in two and three space dimensions. More recently, Yuan and Liu [37] proposed another approach in the discontinuous Galerkin setting based on plane wave basis and local spectral elements.

Higher-order polynomials such as those used in the *hp*-version of FEM and spectral elements are less vulnerable to the pollution effect [3, 4, 38, 39]. In the context of Helmholtz problems, Petersen *et al.* [40] assessed the efficiency of various *p*-FEM shape functions including Lagrange Gauss-Lobatto, integrated Legendre and Bernstein polynomials. They pointed out the advantage of high-order polynomials in reducing the pollution error and the good performance of Bernstein-Bézier FEs in conjunction with Krylov subspace solvers. Further, Lieu *et al.* [41] compared the performance of *p*-FEM, with Lobatto polynomials, and the wave-based discontinuous Galerkin method on various benchmarks. Similarly, El Kacimi *et al.* [42] compared the performance of the Bernstein-Bézier Finite Element method (BBFEM) and PUFEM. It was concluded from these comparative studies that high-order polynomial methods in combination with static condensation are able to deliver comparable or, in some cases, even superior performance. On the other hand, high order *hp*-discontinuous Galerkin methods have been demonstrated as competitive discretisation schemes (see, e.g., [43, 44] and the references cited therein), due to their flexibility in dealing with *hp*-adaptivity and general shaped elements, and their ability in achieving the exponential convergence rate of spectral techniques.

Another alternative to cope with the pollution error is the use of high-order isogeometric elements. The Isogeometric Analysis (IGA) [45] has gained popularity in recent years, due to a number of advantages afforded by spline basis functions, such as exact representation of geometries, higher order continuity and improved convergence properties. This methodology was successfully applied in a number of applications, as e.g. acoustic [46–49], elastodynamic [50–53] and electromagnetic [54–56] waves. Peake *et al.* [57, 58] extended the IGA concept within the framework of boundary elements for exterior acoustic problems, using the partition of unity in two and three space dimensions. They reported superior convergence compared to the partition of unity boundary element method. More recently, Ayala *et al.* [59] studied the performance of the enriched isogeometric collocation method in time-harmonic acoustics. They found improved convergence compared to the isogeometric collocation method. Willberg *et al.* [50] assessed the performance of isogeometric elements with non-uniform rational B-splines (NURBS) against high order SEM and *p*-FEM in Lamb wave propagation analysis.

They concluded that higher order schemes deliver much improved accuracy, with a significant reduction in the total number of degrees of freedom (DoF), compared to conventional FEMs. Moreover, they pointed out that isogeometric elements enable to achieve high convergence rates.

In contrast to standard low order FEMs, where most of the CPU time is spent in the solution process, the computational burden of high order methods shifts to the evaluation of the element matrices and assembling (see, e.g., [60]). Therefore, the design of efficient quadrature rules is crucial to alleviate this major drawback. On tensor product elements, sum factorisation dating back to Orszag [61], has proven fundamental in the efficient implementation of SEMs. This technique relies mainly on a tensor-product structure of the shape functions and enables to achieve near optimal complexity. For simplicial elements, Karniadakis and Sherwin [62] designed special bases preserving a tensor product property. Recently, Ainsworth *et al.* [63] have shown that the Bernstein-Bézier basis naturally possesses the tensorial property needed for the sum factorisation method. They proposed an algorithm to set up the element mass and stiffness matrices with optimal complexity. Kirby and Thinh [64] developed low complexity matrix-free algorithm with Bernstein polynomials for applying the local finite element operators.

The main focus of this paper is to extend BBFEM to accurately solve time-harmonic elastic wave problems. As one of the key ingredients of the method, particular attention is paid to the computation of the element mass and stiffness matrices. Here, analytical rules are used for affine triangular elements and the sum factorisation method together with Stroud quadrature [76] is applied for elements with curved edges, where the geometry of such elements is interpolated via the linear blending map of Gordon and Hall [65–67]. The applicability of BBFEM with a variable polynomial order, using a simple *a priori* indicator, is also investigated throughout a benchmark dealing with the transmission of elastic waves.

The remainder of this paper is organized as follows. Section 2 introduces the model problem and its weak form. The Bernstein-Bézier FE approximation of the governing equations is presented in Section 3. Section 4 gives a description of the analytical and quadrature rules used for evaluating element integrals. Section 5 is devoted to numerical results. Finally, some concluding remarks are made in Section 6.

Notation

The following notation will be used throughout this paper. Each point $\boldsymbol{x}$ in $\mathbb{R}^2$ is identified by its components (x_1, x_2) relative to the Cartesian vector system denoted $(\boldsymbol{e}_1, \boldsymbol{e}_2)$, i.e. $\boldsymbol{x} = x_1\boldsymbol{e}_1 + x_2\boldsymbol{e}_2$. The dot product of two vectors $\boldsymbol{a}$ and $\boldsymbol{b}$ in $\mathbb{C}^2$ is a scalar given by $\boldsymbol{a}\cdot\boldsymbol{b} = \sum_{i=1,2} a_i b_i$. The double dot product of two second-order tensors $\boldsymbol{A}$ and $\boldsymbol{B}$ in $\mathbb{C}^{2\times2}$ is a scalar given by $\boldsymbol{A}:\boldsymbol{B} = \sum_{i,j=1,2} A_{ij}B_{ij}$. The double dot product of a fourth-order tensor $\boldsymbol{C} \in \mathbb{C}^{2\times2}\times\mathbb{C}^{2\times2}$ and a second-order tensor $\boldsymbol{B} \in \mathbb{C}^{2\times2}$ is a second order tensor $\boldsymbol{D} = \boldsymbol{C}:\boldsymbol{B}$ given by $D_{ij} = \sum_{k,l=1,2} C_{ijkl}B_{kl}$. We denote the scalar product either in $\mathbb{C}^2$ or $\mathbb{C}^{2\times2}$ by $(\cdot,\cdot)$, that is, $(\boldsymbol{a},\boldsymbol{b}) = \boldsymbol{a}\cdot\overline{\boldsymbol{b}}$ and $(\boldsymbol{A},\boldsymbol{B}) = \boldsymbol{A}\colon\overline{\boldsymbol{B}}$, where the notation '-' refers to the complex conjugate. The induced norms in $\mathbb{C}^2$ or $\mathbb{C}^{2\times2}$ will be denoted by $\|\cdot\|$.

We also denote the usual inner product on the complex-valued Sobolev space $H^s(D)$, where $s = 0, 1$, by $(\cdot,\cdot)_{s,D}$, with $H^0(D) = L^2(D)$. We keep for simplicity the same notation for the inner products on the space of vector and tensor valued functions $[H^s(D)]^2$ and $[L^2(D)]^{2\times2}$, that is,

$$
\begin{aligned}
(\boldsymbol{u},\boldsymbol{v})_{s,D} &= \sum_{i=1}^{2}(u_i, v_i)_{s,D}, \quad \forall \boldsymbol{u},\boldsymbol{v} \in [H^s(D)]^2,\\
(\boldsymbol{\sigma},\boldsymbol{\tau})_{0,D} &= \sum_{i,j=1}^{2}(\boldsymbol{\sigma}_{ij},\boldsymbol{\tau}_{ij})_{0,D}, \quad \forall \boldsymbol{\sigma},\boldsymbol{\tau} \in [L^2(D)]^{2\times2}.
\end{aligned}
\tag{1.1}
$$

Likewise, for a given $\Sigma \subset \partial D$, the L^2 inner products on $L^2(\Sigma)$ and $[L^2(\Sigma)]^2$ are denoted by $(\cdot,\cdot)_{0,\Sigma}$. We further introduce the induced norm $\|\cdot\|_{s,D}$ in $[H^s(D)]^2$ and the semi-norm $|\cdot|_{1,D}$ in $[H^1(D)]^2$, where $|\boldsymbol{v}|^2_{1,D} = (\boldsymbol{\nabla}\boldsymbol{v},\boldsymbol{\nabla}\boldsymbol{v})_{0,D}$, $\boldsymbol{\nabla} = (\partial_1,\partial_2)^\top$ is the gradient operator, and the superscript '$\top$' denotes the transpose.

Standard multi-index notation will be used. For $\boldsymbol{\alpha} \in \mathbb{Z}_+^3$ and $\boldsymbol{\lambda} \in \mathbb{R}^3$, we set $|\boldsymbol{\alpha}| = \sum_{i=1}^3 \alpha_i$, $\boldsymbol{\lambda}^{\boldsymbol{\alpha}} = \prod_{i=1}^3 \lambda_i^{\alpha_i}$, $\boldsymbol{\alpha}! = \prod_{i=1}^3 \alpha_i!$ and $\binom{|\boldsymbol{\alpha}|}{\boldsymbol{\alpha}} = \frac{|\boldsymbol{\alpha}|!}{\boldsymbol{\alpha}!}$. If $\boldsymbol{\alpha}, \boldsymbol{\beta} \in \mathbb{Z}_+^3$ such that $\boldsymbol{\beta} \geqslant \boldsymbol{\alpha}$, i.e., $\beta_i \geqslant \alpha_i$, $1 \leqslant i \leqslant 3$, $\binom{\boldsymbol{\beta}}{\boldsymbol{\alpha}} = \prod_{i=1}^3 \binom{\beta_i}{\alpha_i}$. We denote by $\mathfrak{e}_i \in \mathbb{Z}_+^3$ the multi-index whose the ith entry is unity and remaining entries are zero.

2 Mathematical model

Let Ω be a bounded Lipschitz domain in $\mathbb{R}^2$, consisting of a solid, homogeneous, isotropic and linear elastic material. We denote by $\Gamma = \partial\Omega$ its boundary, $\boldsymbol{n}$ and $\boldsymbol{t}$ the outward unit normal and tangent vectors to Γ. In the absence of a source, the time harmonic Navier equation reads as [68]

$$-\rho\omega^2 \boldsymbol{u} - \boldsymbol{\nabla} \cdot \boldsymbol{\sigma}(\boldsymbol{u}) = 0 \quad \text{in} \quad \Omega. \tag{2.1}$$

Herein, ω is the angular frequency, ρ is the material density, $\boldsymbol{u}$ is the displacement field and $\boldsymbol{\nabla}\cdot$ is the divergence operator. The Cauchy stress tensor $\boldsymbol{\sigma}(\boldsymbol{u})$ is linearly related to the infinitesimal strain tensor $\boldsymbol{\varepsilon}(\boldsymbol{u})$ by the well-known Hookes law

$$\boldsymbol{\sigma}(\boldsymbol{u}) = \boldsymbol{\mathcal{C}} : \boldsymbol{\varepsilon}(\boldsymbol{u}), \tag{2.2}$$

where

$$\boldsymbol{\varepsilon}(\boldsymbol{u}) = (\boldsymbol{\nabla}\boldsymbol{u} + \boldsymbol{\nabla}\boldsymbol{u}^\top)/2, \tag{2.3}$$

and $\boldsymbol{\mathcal{C}}$ is the fourth order stiffness tensor whose coefficients are given component-wise by

$$\mathcal{C}_{ijkl} = \lambda\delta_{ij}\delta_{kl} + \mu(\delta_{ik}\delta_{jl} + \delta_{il}\delta_{jk}), \qquad 1 \leqslant i, j, k, l \leqslant 2.$$

Herein λ and μ are the Lamé coefficients and δ_{ij} is the Kronecker symbol.

For simplicity, equations (2.1)-(2.3) are completed as in [28,31] by a Robin type boundary condition:

$$\boldsymbol{\sigma}(\boldsymbol{u})\boldsymbol{n} = \mathrm{i}\rho\omega(c_{\mathrm{P}} u_n \boldsymbol{n} + c_{\mathrm{S}} u_t \boldsymbol{t}) + \boldsymbol{g} \quad \text{on} \quad \Gamma, \tag{2.4}$$

where $\mathrm{i} = \sqrt{-1}$ is the imaginary unit number, u_n and u_t are the normal and tangent components of the displacement $\boldsymbol{u}$, respectively, $c_{\mathrm{P}} = \sqrt{\lambda + 2\mu/\rho}$ and $c_{\mathrm{S}} = \sqrt{\mu/\rho}$ are the compressional (P) and shear (S) wave speeds, respectively, and $\boldsymbol{g} \in L^2(\Gamma)$ is a source term.
It is worth mentioning that the boundary condition (2.4), when $\boldsymbol{g} = 0$, corresponds to an absorbing boundary condition of the first order. Here, the source term $\boldsymbol{g}$ is introduced in order to enforce the analytical solution. This enables us to avoid the error due to either the interpolation of curved geometries or the truncation of the infinite domain, when dealing with radiation conditions.

To derive the variational setting of the time-harmonic elastic wave problem (2.1)-(2.4), we multiply (2.1) by the complex conjugate of a test function $\boldsymbol{v} \in \boldsymbol{V} = [H^1(\Omega)]^2$ and integrate by parts over Ω:

$$-\rho\omega^2(\boldsymbol{u}, \boldsymbol{v})_{0,\Omega} + \Big(\boldsymbol{\sigma}(\boldsymbol{u}), \boldsymbol{\nabla}\boldsymbol{v}\Big)_{0,\Omega} - \Big(\boldsymbol{\sigma}(\boldsymbol{u})\boldsymbol{n}, \boldsymbol{v}\Big)_{0,\Gamma} = 0. \tag{2.5}$$

Thus by substituting the Robin boundary condition (2.4) into (2.5) and using the symmetry property of $\boldsymbol{\sigma}(\boldsymbol{u})$, we get the weak form:

$$\begin{cases} \text{Find } \boldsymbol{u} \text{ in } \boldsymbol{V}, \text{ such that} \\ a(\boldsymbol{u}, \boldsymbol{v}) = f(\boldsymbol{v}), \qquad \forall \boldsymbol{v} \in \boldsymbol{V}, \end{cases} \tag{2.6}$$

where $f(\boldsymbol{v}) = (\boldsymbol{g}, \boldsymbol{v})_{0,\Gamma}$, $a(\boldsymbol{u}, \boldsymbol{v}) = a_\Omega(\boldsymbol{u}, \boldsymbol{v}) + a_\Gamma(\boldsymbol{u}, \boldsymbol{v})$ and

$$\begin{aligned} a_\Omega(\boldsymbol{u}, \boldsymbol{v}) &= -\rho\omega^2(\boldsymbol{u}, \boldsymbol{v})_{0,\Omega} + \big(\boldsymbol{\mathcal{C}} : \boldsymbol{\varepsilon}(\boldsymbol{u}), \boldsymbol{\varepsilon}(\boldsymbol{v})\big)_{0,\Omega}, \\ a_\Gamma(\boldsymbol{u}, \boldsymbol{v}) &= -\mathrm{i}\rho\omega\big[c_{\mathrm{P}}(u_n, v_n)_{0,\Gamma} + c_{\mathrm{S}}(u_t, v_t)_{0,\Gamma}\big]. \end{aligned} \tag{2.7}$$

The boundedness of the antilinear and sesquilinear forms $f : \boldsymbol{V} \to \mathbb{C}$ and $a : \boldsymbol{V} \times \boldsymbol{V} \to \mathbb{C}$ follows from the trace theorem and Cauchy-Schwarz inequality. Assume that the coefficients ρ, λ and μ are piece-wise positive constant functions, then it can be seen that the stiffness tensor $\boldsymbol{\mathcal{C}}$ is uniformly positive definite and that the following bounds hold

$$2\mu\|\boldsymbol{\tau}\|^2 \leqslant (\boldsymbol{\mathcal{C}} \colon \boldsymbol{\tau}, \boldsymbol{\tau}) \leqslant 2(\lambda + \mu)\|\boldsymbol{\tau}\|^2, \tag{2.8}$$

for any symmetric tensor $\boldsymbol{\tau} \in \mathbb{C}^{2\times 2}$. Since Ω is assumed to be a bounded Lipschitz domain, Korn's second inequality [69] yields

$$\|\boldsymbol{\varepsilon}(\boldsymbol{v})\|^2_{0,\Omega} \geqslant c_1|\boldsymbol{v}|^2_{1,\Omega} - c_2\|\boldsymbol{v}\|^2_{0,\Omega}, \qquad \forall \boldsymbol{v} \in \boldsymbol{V}, \tag{2.9}$$

where c_1 and c_2 are positive constants. So, it follows that $a : \boldsymbol{V} \times \boldsymbol{V} \to \mathbb{C}$ satisfies Gårding's inequality:

$$\begin{aligned} \operatorname{Re} a(\boldsymbol{v}, \boldsymbol{v}) &= a_\Omega(\boldsymbol{v}, \boldsymbol{v}) = -\rho\omega^2\|\boldsymbol{v}\|^2_{0,\Omega} + \big(\boldsymbol{\mathcal{C}} \colon \boldsymbol{\varepsilon}(\boldsymbol{v}), \boldsymbol{\varepsilon}(\boldsymbol{v})\big)_{0,\Omega} \\ &\geqslant -(\rho\omega^2 + 2\mu c_2)\|\boldsymbol{v}\|^2_{0,\Omega} + 2\mu c_1|\boldsymbol{v}|^2_{1,\Omega}, \qquad \forall \boldsymbol{v} \in \boldsymbol{V}. \end{aligned} \tag{2.10}$$

Thus, the same argument as that of [70] based on the Fredholm alternative [71] and the unique continuation principle for elliptic problems [72], allows to establish the existence and uniqueness for the variational problem (2.6).

3 Bernstein-Bézier FE approximation

Let $\mathscr{T}_h$ be a conforming partition of the domain Ω into triangular elements such that $\overline{\Omega}_h = \cup_{T\in\mathscr{T}_h} T$, where Ω_h is an approximation of Ω and h is the mesh size of $\mathscr{T}_h$ given by $h = \max_{T\in\mathscr{T}_h} h_T$, with $h_T = \operatorname{diam}(T)$. Each $T \in \mathscr{T}_h$ is the image of the triangular master element $\widehat{T}$ defined by

$$\widehat{T} = \big\{\boldsymbol{\xi} = (\xi_1, \xi_2) : \quad 0 \leqslant \xi_1 \leqslant 1, \quad 0 \leqslant \xi_2 \leqslant 1 - \xi_1\big\}, \tag{3.1}$$

i.e. $T = F_T(\widehat{T})$, where F_T is a suitable reference map. For $p \geqslant 1$, let $\boldsymbol{V}_h$ be the finite dimensional approximation space defined by

$$\boldsymbol{V}_h = \Big\{\boldsymbol{v} \in [C^0(\overline{\Omega}_h)]^2 : \quad \boldsymbol{v} \circ F_T \in [\mathbb{P}^p(\widehat{T})]^2, \quad \forall T \in \mathscr{T}_h\Big\},$$

where $\mathbb{P}^p(\widehat{T})$ is the space of polynomials of total degree at most p. Then the discrete analogous expression of the weak form (2.6) is given by

$$\begin{cases} \text{Find } \boldsymbol{u}_h \text{ in } \boldsymbol{V}_h \text{ such that} \\ a_h(\boldsymbol{u}_h, \boldsymbol{v}_h) = f_h(\boldsymbol{v}_h), \qquad \forall \boldsymbol{v}_h \in \boldsymbol{V}_h. \end{cases} \tag{3.2}$$

Here $f_h(\boldsymbol{v}_h) = (\boldsymbol{g}, \boldsymbol{v}_h)_{0,\Gamma_h}$ and $a_h(\boldsymbol{u}_h, \boldsymbol{v}_h) = a_{\Omega_h}(\boldsymbol{u}_h, \boldsymbol{v}_h) + a_{\Gamma_h}(\boldsymbol{u}_h, \boldsymbol{v}_h)$, with

$$\begin{aligned} a_{\Omega_h}(\boldsymbol{u}_h, \boldsymbol{v}_h) &= -\rho\omega^2(\boldsymbol{u}_h, \boldsymbol{v}_h)_{0,\Omega_h} + \Big(\boldsymbol{\mathcal{C}} \colon \boldsymbol{\varepsilon}(\boldsymbol{u}_h), \boldsymbol{\varepsilon}(\boldsymbol{v}_h)\Big)_{0,\Omega_h}, \\ a_{\Gamma_h}(\boldsymbol{u}_h, \boldsymbol{v}_h) &= -\mathrm{i}\rho\omega\Big[c_{\mathrm{P}}(u_n, v_n)_{0,\Gamma_h} + c_{\mathrm{S}}(u_t, v_t)_{0,\Gamma_h}\Big]. \end{aligned} \tag{3.3}$$

Let us consider the barycentric coordinates relative to the master element $\widehat{T}$ defined by

$$\lambda_1(\boldsymbol{\xi}) = \xi_1, \quad \lambda_2(\boldsymbol{\xi}) = \xi_2, \quad \lambda_3(\boldsymbol{\xi}) = 1 - \xi_1 - \xi_2. \tag{3.4}$$

Then the Bernstein polynomials of degree p formulated on the reference element $\widehat{T}$ reads as

$$B^p_{\boldsymbol{\alpha}}(\boldsymbol{\xi}) = \binom{p}{\boldsymbol{\alpha}} \boldsymbol{\lambda}^{\boldsymbol{\alpha}}(\boldsymbol{\xi}), \tag{3.5}$$

where $|\boldsymbol{\alpha}| = p$. These polynomials are linearly independent. Indeed, dividing

$$\sum_{|\boldsymbol{\alpha}|=p} c_{\boldsymbol{\alpha}} \boldsymbol{\lambda}^{\boldsymbol{\alpha}} = 0$$

by λ_3^p gives

$$\sum_{|\boldsymbol{\alpha}|=p} c_{\boldsymbol{\alpha}} x_1^{\alpha_1} x_2^{\alpha_2} = 0,$$

in which $x_i = \xi_i/\lambda_3$. Since the monomials $x_1^{\alpha_1} x_2^{\alpha_2}$ are linearly independent, it follows that all $c_{\boldsymbol{\alpha}}$ are zero. Furthermore, they are $\binom{p+2}{2}$ Bernstein polynomials. Hence, they form a basis for the space $\mathbb{P}^p(\widehat{T})$. It should be noted that Bernstein polynomials are non-negative and form a partition of unity. Moreover, they are only interpolatory at the vertices of $\widehat{T}$.
The approximate Bernstein-Bézier FE solution of (3.2) can be written element-wise in the form

$$\boldsymbol{u}_h(\boldsymbol{x}) = \sum_{|\boldsymbol{\alpha}|=p} B_{\boldsymbol{\alpha}}^p(\boldsymbol{\xi}) \boldsymbol{u}_{\boldsymbol{\alpha}}, \tag{3.6}$$

where the global coordinate $\boldsymbol{x} = F_T(\boldsymbol{\xi})$ and $\{\boldsymbol{u}_{\boldsymbol{\alpha}}\} \subset \mathbb{C}^2$ are the unknown column vectors. An orientation of the element edges enabling the matching edge modes of similar shapes is mandatory to ensure C^0 conformity of high order FEs (see [62, 73] for more details).

The matrix formulation of the discrete weak form (3.2) can be written as

$$\mathsf{A}\mathsf{y} = \mathsf{b}, \tag{3.7}$$

where A is a $n_{\text{dof}} \times n_{\text{dof}}$ sparse, complex symmetric matrix and b is the right-hand side column vector of $\mathbb{C}^{n_{\text{dof}}}$ and n_{dof} is the total number of DoF and y is the unknown column vector of dimension DoF. The global matrix A and the right-hand side vector b are evaluated by assembling the element contributions A^T and b^T. The element matrix can be written as

$$\mathsf{A}^T = -\rho\omega^2 \mathsf{M}^T + \mathsf{K}^T - \mathrm{i}\rho\omega \mathsf{S}^T. \tag{3.8}$$

Let us denote by $\mathscr{N}_L$ the mapping from the indices $(k, \boldsymbol{\gamma})$ in the local FE basis

$$\cup_{|\boldsymbol{\gamma}|=p} \{ B_{\boldsymbol{\gamma}}^p \boldsymbol{e}_k : k = 1, 2 \}$$

to the local DoF number $\mathscr{N}_L(k, \boldsymbol{\gamma})$. Let set $i = \mathscr{N}_L(i_1, \boldsymbol{\alpha})$ and $j = \mathscr{N}_L(i_2, \boldsymbol{\beta})$, where $1 \leqslant i_1, i_2 \leqslant 2$ and $|\boldsymbol{\alpha}| = |\boldsymbol{\beta}| = p$. Then, the entries of the element matrices M^T and K^T are given by

$$\mathsf{M}_{ij}^T = \delta_{i_1 i_2} \big(|\mathsf{J}_T| \, B_{\boldsymbol{\beta}}^p, B_{\boldsymbol{\alpha}}^p \big)_{0,\widehat{T}}, \tag{3.9}$$

$$\mathsf{S}_{ij}^T = \sum_{\mathcal{E} \subset T \cap \Gamma_h} \big(l_{\mathcal{E}} \big[c_{\mathrm{P}} n_{i_1}^{\mathcal{E}} n_{i_2}^{\mathcal{E}} + c_{\mathrm{S}} t_{i_1}^{\mathcal{E}} t_{i_2}^{\mathcal{E}} \big] B_{\boldsymbol{\beta}}^p, B_{\boldsymbol{\alpha}}^p \big)_{0,\widehat{I}}, \tag{3.10}$$

$$\mathsf{K}_{ij}^T = \big(|\mathsf{J}_T| \, \boldsymbol{\mathcal{C}} \colon \boldsymbol{\varepsilon}(B_{\boldsymbol{\beta}}^p \boldsymbol{e}_{i_2}), \boldsymbol{\varepsilon}(B_{\boldsymbol{\alpha}}^p \boldsymbol{e}_{i_1}) \big)_{0,\widehat{T}}, \tag{3.11}$$

with $\boldsymbol{n}^{\mathcal{E}} = n_1^{\mathcal{E}} \boldsymbol{e}_1 + n_2^{\mathcal{E}} \boldsymbol{e}_2$, $\boldsymbol{t}^{\mathcal{E}} = t_1^{\mathcal{E}} \boldsymbol{e}_1 + t_2^{\mathcal{E}} \boldsymbol{e}_2$ and $|\boldsymbol{\alpha}| = |\boldsymbol{\beta}| = p$. Here, $\mathsf{J}_T = \left(\frac{\mathrm{D}F_T}{\mathrm{D}\boldsymbol{\xi}} \right)^\top$ denotes the Jacobian matrix, $|\mathsf{J}_T|$ its determinant, $\mathcal{E}$ is an edge of T and $l_{\mathcal{E}} = \sqrt{x'^2_1(s) + x'^2_2(s)}$, with $s \in \widehat{I} = [0, 1] = F_T^{-1}(\mathcal{E})$. For the element right hand side b^T, its entries are defined by

$$\mathsf{b}_i^T = \sum_{\mathcal{E} \subset T \cap \Gamma_h} \big(l_{\mathcal{E}} \boldsymbol{g} \cdot \boldsymbol{e}_{i_1}, B_{\boldsymbol{\alpha}}^p \big)_{0,\widehat{I}}. \tag{3.12}$$

By setting

$$\mathsf{M}_{\boldsymbol{\alpha},\boldsymbol{\beta}}^p = \big(|\mathsf{J}_T| \, B_{\boldsymbol{\beta}}^p, B_{\boldsymbol{\alpha}}^p \big)_{0,\widehat{T}}, \tag{3.13}$$

we have $\mathsf{M}^T_{ij} = \delta_{i_1 i_2}\mathsf{M}^p_{\boldsymbol{\alpha},\boldsymbol{\beta}}$. From the view point of implementation in the FEM, it is customary to use engineering notation when evaluating the element stiffness matrix. The components of the strain tensor are then rearranged into a column vector $\boldsymbol{\varepsilon}(\boldsymbol{v}) = [\varepsilon_{11}(\boldsymbol{v}), \varepsilon_{22}(\boldsymbol{v}), 2\varepsilon_{12}(\boldsymbol{v})]^\top$. Following [74], it can be shown that

$$\mathsf{K}^T_{ij} = \left(|\mathsf{J}_T|\ \boldsymbol{\mathcal{D}}\ \boldsymbol{\varepsilon}(B^p_{\boldsymbol{\beta}}\boldsymbol{e}_{i_2}), \boldsymbol{\varepsilon}(B^p_{\boldsymbol{\alpha}}\boldsymbol{e}_{i_1})\right)_{0,\widehat{T}}. \tag{3.14}$$

The applications dealt with herein fall in the plane strain setting. The expression of the second order tensor $\boldsymbol{\mathcal{D}}$ can be found in textbooks, for example [74].
Let us denote by $\mathsf{J}^{-1}_{T,k}$ the kth row of the inverse matrix J^{-1}_T and set

$$\mathscr{G}_T(\boldsymbol{w}) = \begin{bmatrix} \mathsf{J}^{-1}_{T,1}\boldsymbol{w} & 0 \\ 0 & \mathsf{J}^{-1}_{T,2}\boldsymbol{w} \\ \mathsf{J}^{-1}_{T,2}\boldsymbol{w} & \mathsf{J}^{-1}_{T,1}\boldsymbol{w} \end{bmatrix}, \tag{3.15}$$

for a given column vector $\boldsymbol{w}$ in $\mathbb{R}^2$. Then, by noting that

$$\boldsymbol{\varepsilon}(B^p_{\boldsymbol{\alpha}}\boldsymbol{e}_k) = \begin{bmatrix} \partial_1 B^p_{\boldsymbol{\alpha}} & 0 \\ 0 & \partial_2 B^p_{\boldsymbol{\alpha}} \\ \partial_2 B^p_{\boldsymbol{\alpha}} & \partial_1 B^p_{\boldsymbol{\alpha}} \end{bmatrix} \boldsymbol{e}_k = \mathscr{G}_T(\widehat{\boldsymbol{\nabla}} B^p_{\boldsymbol{\alpha}})\ \boldsymbol{e}_k, \tag{3.16}$$

where $\widehat{\boldsymbol{\nabla}}$ is the gradient operator with respect to the local coordinate $\boldsymbol{\xi}$, equation (3.14) can be written as

$$\mathsf{K}^T_{ij} = \left(|\mathsf{J}_T|\boldsymbol{\mathcal{D}}\ \mathscr{G}_T(\widehat{\boldsymbol{\nabla}} B^p_{\boldsymbol{\beta}})\ \boldsymbol{e}_{i_2}, \mathscr{G}_T(\widehat{\boldsymbol{\nabla}} B^p_{\boldsymbol{\alpha}})\ \boldsymbol{e}_{i_1}\right)_{0,\widehat{T}}. \tag{3.17}$$

The next section describes the computation procedures for evaluating the element integrals involved in the element matrices and right hand side vectors.

4 Computation of element integrals

This section is devoted to the computation strategies of the element matrices and right hand side vectors of the stated problem. For ease of presentation, we suppose the polynomial order p to be uniform.

4.1 Case of elements with straight edges

Interior elements in the computational mesh grid are often taken with straight edges. Hence, in this case, F_T reduces to a standard linear FE map and the analytical integration rules described in [63,64] can be used. Bernstein polynomials possess some nice properties, namely the integral of a Bernstein polynomial on a simplex has a simple form, which reads in two-dimensional space on the reference triangle $\widehat{T}$, as

$$\int_{\widehat{T}} B^n_{\boldsymbol{\alpha}}\ \mathrm{d}\boldsymbol{\xi} = \frac{|\widehat{T}|}{\binom{n+2}{2}}, \quad |\boldsymbol{\alpha}| = n. \tag{4.1}$$

Moreover, the product of two Bernstein polynomials is, up to a scaling factor, a Bernstein polynomial. More precisely, we have

$$B^n_{\boldsymbol{\alpha}} B^m_{\boldsymbol{\beta}} = \frac{\binom{\boldsymbol{\alpha}+\boldsymbol{\beta}}{\boldsymbol{\alpha}}}{\binom{n+m}{m}} B^{n+m}_{\boldsymbol{\alpha}+\boldsymbol{\beta}}, \quad \text{with} \quad |\boldsymbol{\alpha}| = n, |\boldsymbol{\beta}| = m. \tag{4.2}$$

Hence, thanks to (4.1), simple algebra shows that

$$\mathsf{M}^p_{\boldsymbol{\alpha},\boldsymbol{\beta}} = \frac{|T|}{|\widehat{T}|}\int_{\widehat{T}} B^{2p}_{\boldsymbol{\alpha}+\boldsymbol{\beta}}\ \mathrm{d}\boldsymbol{\xi} = \frac{|T|}{\binom{2p+2}{2}} c_{\boldsymbol{\alpha},\boldsymbol{\beta}}, \tag{4.3}$$

where the coefficients $c_{\boldsymbol{\alpha},\boldsymbol{\beta}} = \frac{\binom{\boldsymbol{\alpha}+\boldsymbol{\beta}}{\boldsymbol{\alpha}}}{\binom{2p}{p}}$ are evaluated as in [63], based on the procedure described below:

Algorithm 1 Evaluation of the multinomial coefficients

Compute and store all the binomial coefficients $\binom{n+m}{m}$, $0 \leqslant n, m \leqslant 2p$, using Pascal's formula.
for $\alpha_1 = 0$ to p **do**
  for $\beta_1 = 0$ to p **do**
    $c \leftarrow \binom{\alpha_1+\beta_1}{\alpha_1} / \binom{2p}{p}$;
    for $\alpha_2 = 0$ to $p - \alpha_1$ **do**
      for $\beta_2 = 0$ to $p - \beta_1$ **do**
        $d \leftarrow c \times \binom{\alpha_2+\beta_2}{\alpha_2}$;
        $c_{\boldsymbol{\alpha},\boldsymbol{\beta}} \leftarrow d \times \binom{p-\alpha_1-\alpha_2+p-\beta_1-\beta_2}{p-\alpha_1-\alpha_2}$.
      end for
    end for
  end for
end for

Using Algorithm 1, the cost to set up the element mass matrix is $\mathcal{O}(p^4)$.
Additionally, the gradient of Bernstein polynomials can be written as

$$\widehat{\boldsymbol{\nabla}} B^p_{\boldsymbol{\alpha}} = p \sum_{k=1}^{3} B^{p-1}_{\boldsymbol{\alpha}_k} \widehat{\boldsymbol{\nabla}} \lambda_k, \tag{4.4}$$

where $\boldsymbol{\alpha}_k = \boldsymbol{\alpha} - \mathfrak{e}_k$ and $B^{p-1}_{\boldsymbol{\alpha}_k} = 0$ if $\boldsymbol{\alpha}_k$ has a negative component. Thanks to (3.17), these lead to a closed form for the element stiffness entries:

$$\mathsf{K}^T_{ij} \;=\; p^2 \sum_{k,l=1}^{3} \left[[\mathscr{G}_T(\widehat{\boldsymbol{\nabla}} \lambda_k)]^\top \boldsymbol{\mathcal{D}}\, \mathscr{G}_T(\widehat{\boldsymbol{\nabla}} \lambda_l) \right]_{i_1,i_2} \mathsf{M}^{p-1}_{\boldsymbol{\alpha}_k,\boldsymbol{\beta}_l}, \tag{4.5}$$

where the quantities $\mathsf{M}^{p-1}_{\boldsymbol{\alpha}_k,\boldsymbol{\beta}_l}$ can be deduced from expression (4.3). It is noteworthy that the above analytical rules apply in the case of piecewise constant coefficients.

4.2 Case of elements with curved edges

The element contributions S^T_i and b^T_i, reducing to edge integrals, are evaluated using a high order Gauss-Legendre quadrature, for any element T sharing an edge $\mathcal{E}$ with the curved boundary Γ_h. The geometry of such elements is interpolated with the six-noded Lagrange map, i.e.

$$F_T(\boldsymbol{\xi}) \;=\; \sum_i \lambda_i(\boldsymbol{\xi})(2\lambda_i(\boldsymbol{\xi}) - 1)\boldsymbol{q}_i + 4 \sum_{i<j} \lambda_i(\boldsymbol{\xi})\lambda_j(\boldsymbol{\xi})\boldsymbol{q}_{ij}, \tag{4.6}$$

where the definition of the nodal points $\{\boldsymbol{q}_i\}$ and $\{\boldsymbol{q}_{ij}\}$ of T is given in Figure 1. Since the analytical solution is enforced by the Robin boundary condition (2.4), the error due to the interpolation of the geometry does not affect the overall discretisation error, as the computed numerical solution would be compared to the imposed analytical one.

Interior elements with curved edges may be encountered as well in some applications, as for example, in elastic wave transmission problems dealt with in the present work. In such applications, an interface-fitted mesh grid is needed, and the Lagrange map (4.6) may result in a significant error [75], especially on coarse mesh grids with high polynomial order. To account here for curved geometries, we use the linear blending map method of Gordon and Hall [65–67]. Suppose there is an element with a curved edge, described by its parametric form $\boldsymbol{q} = \boldsymbol{q}(s)$, where $0 \leqslant s \leqslant 1$, and that this edge is $(\boldsymbol{q}_1, \boldsymbol{q}_2)$, with $\boldsymbol{q}(0) = \boldsymbol{q}_1$ and $\boldsymbol{q}(1) = \boldsymbol{q}_2$ (see Figure 1). Then this map can be defined as

$$F_T(\boldsymbol{\xi}) = \lambda_1(\xi)\boldsymbol{q}_1 + \lambda_2(\xi)\boldsymbol{q}_2 + \lambda_3(\xi)\boldsymbol{q}_3 + \frac{\lambda_1(\xi)\lambda_2(\xi)}{\xi_2\,(1-\xi_2)} \left[\boldsymbol{q}\,(\xi_2) - ((1-\xi_2)\,\boldsymbol{q}_1 + \xi_2 \boldsymbol{q}_2) \right]. \tag{4.7}$$

It should be noted that this method can also be applied to elements with many curved edges [67]. In the sequel, we will make use of the Gauss-Jacobi quadrature defined by

$$\int_0^1 (1-\eta)^a \eta^b f(\eta)\, \mathrm{d}\eta \simeq \sum_{r=0}^{q} w_r^{(a,b)} f(\eta_r^{(a,b)}), \tag{4.8}$$

where the nodes $\{\eta_r^{(a,b)}\}$ are located in the open interval $(0,1)$ and the weights $\{w_r^{(a,b)}\}$ are all positive, with $a, b > -1$.

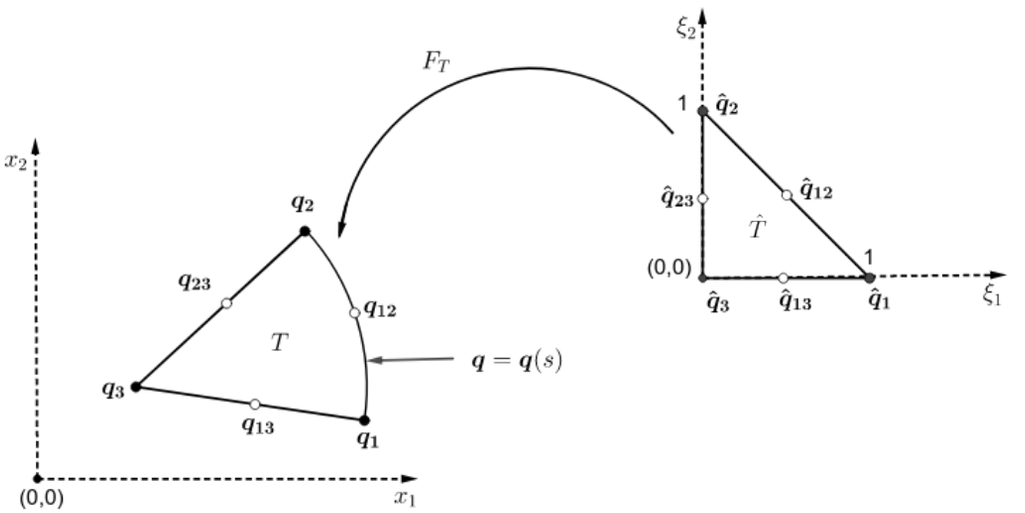

Figure 1: Reference map for a curved triangular element.

Suppose, for example, that edge $\mathcal{E}$ is edge $(\boldsymbol{q}_1, \boldsymbol{q}_2)$ (see Figure 1). Then $B_{\boldsymbol{\alpha}}^p$ reduces to a univariate Bernstein polynomial on the unit interval $\widehat{I}$. More precisely, we have $B_{\boldsymbol{\alpha}}^p(\boldsymbol{\xi}) = B_{\alpha_2}^p(\xi_2)$, with $\boldsymbol{\alpha} = (\alpha_1, \alpha_2, 0)$. Thus applying the above quadrature rule, with $a = b = 0$ corresponding to the well-known Gauss-Legendre rule, the edge contribution in (3.12), denoted by $\mathsf{b}_i^{T,\mathcal{E}}$, can be approximated as

$$\mathsf{b}_i^{T,\mathcal{E}} = \left(l_{\mathcal{E}} \boldsymbol{e}_{i_1} \cdot \boldsymbol{g}, B_{\boldsymbol{\alpha}}^p\right)_{0,\widehat{I}} \simeq \sum_{r=1}^{q} w_r^{(0,0)} l_{\mathcal{E}}(\eta_r^{(0,0)}) B_{\alpha_2}^p(\eta_r^{(0,0)})\ \boldsymbol{e}_{i_1} \cdot \boldsymbol{g}(\boldsymbol{x}_r), \tag{4.9}$$

where $\boldsymbol{x}_r = F_T(1-\eta_r^{(0,0)}, \eta_r^{(0,0)})$. In a similar way, for the edge contribution in (3.10), we have

$$\begin{aligned} \mathsf{S}_{ij}^{T,\mathcal{E}} &= \left(l_{\mathcal{E}}\left[c_{\mathrm{P}} n_{i_1}^{\mathcal{E}} n_{i_2}^{\mathcal{E}} + c_{\mathrm{S}} t_{i_1}^{\mathcal{E}} t_{i_2}^{\mathcal{E}}\right] B_{\boldsymbol{\beta}}^p, B_{\boldsymbol{\alpha}}^p\right)_{0,\widehat{I}} \\ &\simeq \sum_{r=1}^{q} w_r^{(0,0)} l_{\mathcal{E}}(\eta_r^{(0,0)}) \left[\left(c_{\mathrm{P}} n_{i_1}^{\mathcal{E}} n_{i_2}^{\mathcal{E}} + c_{\mathrm{S}} t_{i_1}^{\mathcal{E}} t_{i_2}^{\mathcal{E}}\right)(\boldsymbol{x}_r)\right] B_{\alpha_2}^p(\eta_r^{(0,0)}) B_{\beta_2}^p(\eta_r^{(0,0)}), \end{aligned} \tag{4.10}$$

in which $\boldsymbol{\beta} = (\beta_1, \beta_2, 0)$. The approximate edge integrals given by (4.9) and (4.10) require the evaluation of univariate Bernstein polynomials B_α^p, for all $\alpha = 0, \cdots, p$, on the Gauss-Legendre quadrature points $\{\eta_r^{(0,0)}\}$. They are computed based on the recursion formula

$$B_\alpha^{m+1}(\eta) = \eta B_{\alpha-1}^m(\eta) + (1-\eta) B_\alpha^m(\eta), \tag{4.11}$$

where $B_{-1}^m = B_{m+1}^m = 0$ and $B_0^0 = 1$. These translate into the following algorithm:

Algorithm 2 Evaluation of the univariate of Bernstein polynomials.

$B_0^0(\eta) \leftarrow 1$;
for $n = 1$ to p **do**
  $B_0^n(\eta) \leftarrow (1-\eta) \times B_0^{n-1}(\eta)$;
end for
for $n = 1$ to p **do**
  for $m = n$ to p **do**
    $B_n^m(\eta) \leftarrow \eta \times B_{n-1}^{m-1}(\eta) + (1-\eta) \times B_n^{m-1}(\eta)$.
  end for
end for

It remains to evaluate numerically the element integrals defined by (3.13) and (3.17). For this purpose, we introduce the Duffy transform which maps the unit square $\widehat{S} = \widehat{I} \times \widehat{I}$ with coordinates $\boldsymbol{\eta} = (\eta_1, \eta_2)$ to the reference triangle $\widehat{T}$:

$$\boldsymbol{\xi} = F(\boldsymbol{\eta}) = (\eta_1, (1-\eta_1)\eta_2)^\top . \tag{4.12}$$

This transformation yields a tensorial construction of the Bernstein-Bézier basis on simplices. Hence, sum-factorisation can be applied to efficiently evaluate and integrate Bernstein polynomials [63]. In particular, the case of two space variables gives

$$B_{\boldsymbol{\alpha}}^p(\boldsymbol{\xi}) = B_{\alpha_1}^p(\eta_1) B_{\alpha_2}^{p-\alpha_1}(\eta_2). \tag{4.13}$$

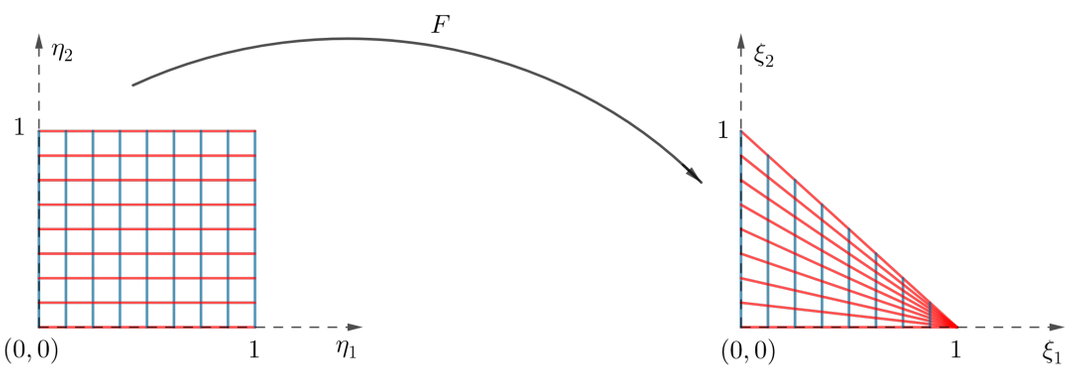

Figure 2: Reference triangular element and unit square.

Taking advantage of the key property (4.13) and the transformation (4.12), the element mass integrals in (3.13) become

$$\mathsf{M}_{\boldsymbol{\alpha},\boldsymbol{\beta}}^p = \int_0^1 \Big(\int_0^1 |\mathsf{J}_T| B_{\alpha_1}^p(\eta_1) B_{\beta_1}^p(\eta_1)(1-\eta_1)\, \mathrm{d}\eta_1 \Big) B_{\alpha_2}^{p-\alpha_1}(\eta_2) B_{\beta_2}^{p-\beta_1}(\eta_2)\, \mathrm{d}\eta_2. \tag{4.14}$$

So, making use of the Stroud quadrature rule [76] in conjunction with the Gauss-Jacobi quadrature (4.8) gives

$$\begin{aligned} \mathsf{M}_{\boldsymbol{\alpha},\boldsymbol{\beta}}^p \;\simeq\; & \sum_{s=1}^{q} w_s^{(0,0)} B_{\alpha_2}^{p-\alpha_1}(\eta_s^{(0,0)}) B_{\beta_2}^{p-\beta_1}(\eta_s^{(0,0)}) \times \\ & \Big(\sum_{r=1}^{q} g_{rs}\; w_r^{(1,0)} B_{\alpha_1}^p(\eta_r^{(1,0)}) B_{\beta_1}^p(\eta_r^{(1,0)}) \Big), \end{aligned} \tag{4.15}$$

where $g_{rs} = |\mathsf{J}_T(\boldsymbol{\xi}_{rs})|$,

$$\boldsymbol{\xi}_{rs} = F(\boldsymbol{\eta}_{rs}) \quad \text{and} \quad \boldsymbol{\eta}_{rs} = (\eta_r^{(1,0)}, \eta_s^{(0,0)})^\top. \tag{4.16}$$

A routine evaluating the element mass entry $\mathsf{M}^p_{\boldsymbol{\alpha},\boldsymbol{\beta}}$ is described below:

Algorithm 3 Evaluation of the entry $\mathsf{M}^p_{\boldsymbol{\alpha},\boldsymbol{\beta}}$.

$\mathsf{M}^p_{\boldsymbol{\alpha},\boldsymbol{\beta}} \leftarrow 0$;
for $s = 1$ to q **do**
  $c_{(s,\alpha_1,\beta_1)} \leftarrow 0$;
  for $r = 1$ to q **do**
    $c_{(s,\alpha_1,\beta_1)} \leftarrow c_{(s,\alpha_1,\beta_1)} + g_{rs} \times w_r^{(1,0)} \times B^p_{\alpha_1}(\eta_r^{(1,0)}) \times B^p_{\beta_1}(\eta_r^{(1,0)})$;
  end for
  $\mathsf{M}^p_{\boldsymbol{\alpha},\boldsymbol{\beta}} \leftarrow \mathsf{M}^p_{\boldsymbol{\alpha},\boldsymbol{\beta}} + c_{(s,\alpha_1,\beta_1)} \times w_s^{(0,0)} \times B^{p-\alpha_1}_{\alpha_2}(\eta_s^{(0,0)}) \times B^{p-\beta_1}_{\beta_2}(\eta_s^{(0,0)})$;
end for

The element mass matrix consists of $\mathcal{O}(p^4)$ entries and the evaluation of the auxiliary field $(c_{(s,\alpha_1,\beta_1)})$ (see Algorithm 3) requires $\mathcal{O}(qp^2)$ floating point operations. Thus, the cost to set up the element mass matrix is $\mathcal{O}(qp^2) + \mathcal{O}(qp^4)$. However, the required number q q of quadrature points to perform a sufficiently accurate numerical integration should be chosen such that $q = \mathcal{O}(p)$. Therefore, the total cost is $\mathcal{O}(p^5)$. It is worth noticing that a naive evaluation of the element mass matrix will results in $\mathcal{O}(p^6)$ operations. The key idea to achieve a low operation count in the assembly of the element matrices is the use of the tensorial construction of the Bernstein-Bézier basis (4.13) combined with sum-factorisation. This technique is considered to be a crucial factor in the efficient implementation of high order p-FEMs and SEMs [62]. Fast algorithms achieving optimal complexity can be found in References [63, 77]. But they are not considered here.
The analogous expression of (3.17) with a non constant Jacobian can be written as

$$\mathsf{K}^T_{ij} = p^2 \sum_{k,l=1}^{3} \left(|\mathsf{J}_T| \Big[[\mathscr{G}_T(\widehat{\boldsymbol{\nabla}}\lambda_k)]^\top \boldsymbol{\mathcal{D}}\, \mathscr{G}_T(\widehat{\boldsymbol{\nabla}}\lambda_l) \Big]_{i_1,i_2} B^{p-1}_{\boldsymbol{\beta}_l}, B^{p-1}_{\boldsymbol{\alpha}_k} \right)_{0,\widehat{T}}. \tag{4.17}$$

Thus, by setting

$$g_{(i_1,i_2,k,l)} = |\mathsf{J}_T| \Big[[\mathscr{G}_T(\widehat{\boldsymbol{\nabla}}\lambda_k)]^\top \boldsymbol{\mathcal{D}}\, \mathscr{G}_T(\widehat{\boldsymbol{\nabla}}\lambda_l) \Big]_{i_1,i_2}, \tag{4.18}$$

and using once again property (4.13) and the Duffy transform (4.12), we get

$$\begin{aligned}
\mathsf{K}^T_{ij} &= p^2 \sum_{k,l=1}^{3} \left(g_{(i_1,i_2,k,l)} B^{p-1}_{\boldsymbol{\beta}_l}, B^{p-1}_{\boldsymbol{\alpha}_k} \right)_{0,\widehat{T}} \\
&= p^2 \sum_{k,l=1}^{3} \int_0^1 \Big(\int_0^1 g_{(i_1,i_2,k,l)} B^{p-1}_{\alpha_{k,1}}(\eta_1) B^{p-1}_{\beta_{l,1}}(\eta_1)(1-\eta_1)\, \mathrm{d}\eta_1 \Big) \quad \times \\
&\qquad\qquad B^{p-1-\alpha_{k,1}}_{\alpha_{k,2}}(\eta_2) B^{p-1-\beta_{l,1}}_{\beta_{l,2}}(\eta_2)\, \mathrm{d}\eta_2,
\end{aligned} \tag{4.19}$$

where $(\alpha_{k,1}, \alpha_{k,2}, p-1-\alpha_{k,1}-\alpha_{k,2}) = \boldsymbol{\alpha}_k$ and $(\beta_{l,1}, \beta_{l,2}, p-1-\beta_{l,1}-\beta_{l,2}) = \boldsymbol{\beta}_l$. These give, by applying the Stroud quadrature rule,

$$\begin{aligned}
\mathsf{K}^T_{ij} \simeq p^2 \sum_{k,l=1}^{3} \Bigg[\sum_{s=1}^{q} w_s^{(0,0)} B^{p-1-\alpha_{k,1}}_{\alpha_{k,2}}(\eta_s^{(0,0)}) B^{p-1-\beta_{l,1}}_{\beta_{l,2}}(\eta_s^{(0,0)}) \quad \times \\
\left(\sum_{r=1}^{q} g^{rs}_{(i_1,i_2,k,l)} w_r^{(1,0)} B^{p-1}_{\alpha_{k,1}}(\eta_r^{(1,0)}) B^{p-1}_{\beta_{l,1}}(\eta_r^{(1,0)}) \right) \Bigg],
\end{aligned} \tag{4.20}$$

in which the auxiliary field $g^{rs}_{(i_1,i_2,k,l)}$ refers to the evaluation of the right hand side in equation (4.18) at the Stroud quadrature points $\{\boldsymbol{\xi}_{rs}\}$, defined by equation (4.16). From the above formula, it can be seen that the cost to set up the element stiffness matrix is $\mathcal{O}(p^5)$. It should be noted that the proposed quadrature rules also work in the case of variable coefficients.

5 Numerical results

In this section, numerical results are presented to assess the performance of the proposed approach on various two dimensional benchmark problems. The BBFEM is efficiently implemented via static condensation such that the internal DoF are eliminated at the element level. This leads to a condensed linear system involving only DoF attached the mesh skeleton. Once the solution related to the vertex and edge modes is computed, the internal DoF can be recovered at the post-processing stage by solving element-wise local small linear problems. This procedure enables a substantial reduction of the size of the global system matrix and its bandwidth. The resulting condensed linear system is assembled in an element-by-element fashion, based on coordinate storage format, and solved by using the multi-frontal sparse direct solver `MUMPS` [78]. The latter is interfaced with `METIS` package [79] in order to reduce the bandwidth and the extra fill-in of the global matrix.
The accuracy of BBFEM is assessed by the following L^2 error

$$\epsilon_2 = \frac{\|\boldsymbol{u}_h - \boldsymbol{u}\|_{0,\Omega_h}}{\|\boldsymbol{u}\|_{0,\Omega_h}} \times 100\%. \tag{5.1}$$

In the sequel, we will denote by $\mathrm{Re}(\boldsymbol{u}_h)$ the real part of the approximate displacement field $\boldsymbol{u}_h$ and by $|\mathrm{Re}(\boldsymbol{u}_h)|$ the corresponding Euclidean norm. We will use the same notations as in (3.7) for the statically condensed matrix and right hand side. The wave resolution, in the case of homogeneous media, can be defined by the parameters

$$\tau_{\mathrm{P}} = \lambda_{\mathrm{P}}\sqrt{\frac{n_{\mathrm{dof}}}{|\Omega_h|}} \quad \text{and} \quad \tau_{\mathrm{S}} = \lambda_{\mathrm{S}}\sqrt{\frac{n_{\mathrm{dof}}}{|\Omega_h|}}, \tag{5.2}$$

giving the numbers of DoF per P and S wavelengths λ_{P} and λ_{S}, respectively. Herein, n_{dof} is the total number of DoF of the condensed linear system and $|\Omega_h|$ is the surface area of the approximate elastic domain Ω_h.

We will denote by nnz the number of non zero entries in the condensed global matrix, and by κ_A the condition number of the resulting condensed linear system, evaluated by `MUMPS` using the metric defined in [80] by

$$\kappa_A = \frac{||\ |A|\ |A^{-1}|\ |\hat{x}|\ +\ |A^{-1}|\ |b|\ ||_\infty}{||\hat{x}||_\infty}. \tag{5.3}$$

Herein $\hat{x}$ is the computed solution, $||\cdot||_\infty$ is the usual l_∞ norm, $|A| = (|a_{ij}|)$ and $|b| = (|b_i|)$. The above defined quantities are used in the following numerical analysis to assess the performance of the BBFEM modelling in solving various elastic wave problems.

The next subsection is devoted to a performance study of the computation procedures used for evaluating the local mass and stiffness matrices.

5.1 Computation of element matrices: performance and timing results

We present here some numerical results that compare the CPU times of the standard quadrature, sum factorization based quadrature and analytical rules. The local mass and stiffness matrices are evaluated on a single mesh element, with straight edges. All the computations are performed in double precision on an Intel Core i5 CPU Laptop (with 2.70GHz $\times$ 2).

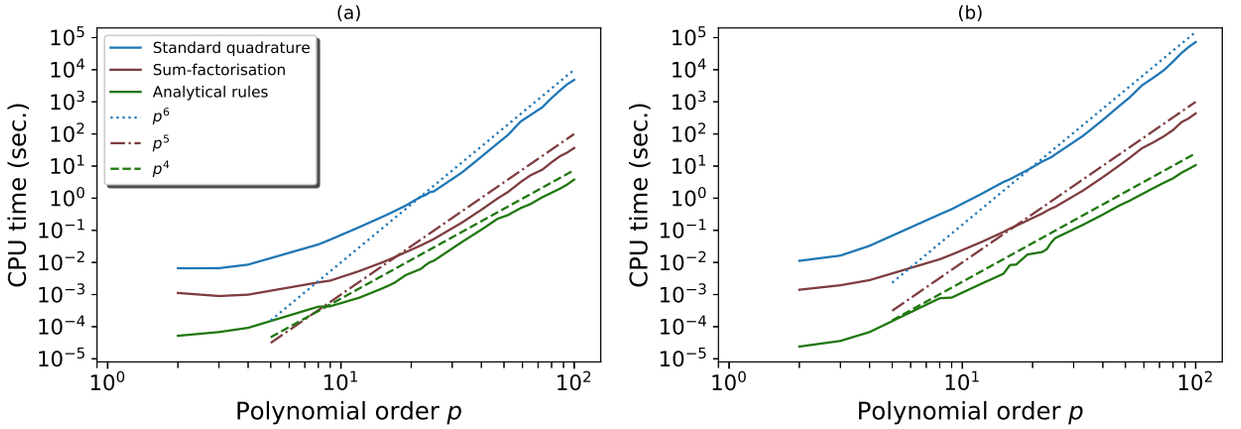

Figure 3: CPU time needed for the evaluation of element matrices: (a) element mass matrix and (b) element stiffness matrix.

Figure 3 displays the CPU time needed to set up the element mass and stiffness matrices versus the polynomial degree p, for each procedure. The above results show clearly that the standard quadrature, sum-factorization based quadrature and analytical rules yield, respectively, $\mathcal{O}(p^4)$, $\mathcal{O}(p^5)$ and $\mathcal{O}(p^6)$ operations. These confirm the predicted complexity costs discussed in Section 3. As expected, analytic rules outperform the other integration procedures. Moreover, the cost of sum-factorization based quadrature is at least one order of magnitude below that of the standard quadrature.

A description of the benchmark tests dealt with and numerical results are given in the next subsections.

5.2 Harmonic elastic waves from a pulsating cavity

5.2.1 Description of the problem

This first benchmark concerns the propagation of harmonic waves generated from an infinite cylindrical cavity of radius a in an elastic medium subject to a uniform harmonically varying stress, where the traction $\boldsymbol{T} = \boldsymbol{\sigma}(\boldsymbol{u})\boldsymbol{n}$ is prescribed on the cavity boundary. The computational domain Ω has an annular shape with inner and outer radii a and $R = 2a$, respectively (see Figure 4).

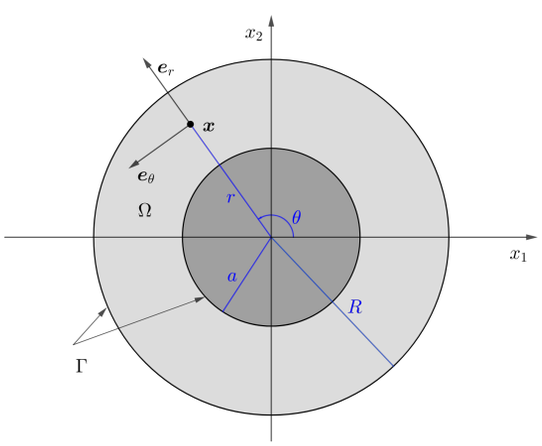

Figure 4: Computational domain and problem specification.

A compression stress of amplitude p_0, i.e., $\boldsymbol{T} = -p_0\boldsymbol{e}_r$ gives rise to a purely propagating compression

wave expressed in terms of the displacement field as [68]

$$\boldsymbol{u} = \frac{aH_0'(k_{\mathrm{P}}r)\,p_0}{(\lambda+2\mu)k_{\mathrm{P}}aH_0(k_{\mathrm{P}}a)+2\mu H_0'(k_{\mathrm{P}}a)}\mathbf{e}_r, \tag{5.4}$$

while a shear stress with a prescribed traction $\boldsymbol{T} = -\sigma_0\boldsymbol{e}_\theta$ produces a purely propagating shear wave for which the displacement field is given by

$$\boldsymbol{u} = -\frac{aH_0'(k_{\mathrm{S}}r)\,\sigma_0}{\mu\zeta_{\mathrm{S}}H_0(k_{\mathrm{S}}a)+2\mu H_0'(k_{\mathrm{S}}a)}\mathbf{e}_\theta. \tag{5.5}$$

Herein, H_0 is the Hankel function of the first kind and zero order and the prime denotes a derivative with respect to the argument.

In this example, which serves to study the convergence of h and p versions of BBFEM, we will use the parameters summarized in Table 1, where the elastic properties of the medium are taken to be those of Aluminium.

	Description	Value
p_0	Compression stress amplitude [N/m^2]	10^{13}
σ_0	Shear stress amplitude [N/m^2]	10^{13}
a	Cavity radius [m]	1
E	Young's modulus [N/m^2]	69×10^9
ν	Poisson's ratio	0.32
ρ	Density [kg/m^3]	2700

Table 1: Parameters used in the pulsating cavity problem

Hence, the P and S wave speeds are $c_{\mathrm{P}} = 6047.26$m/s and $c_{\mathrm{S}} = 3111.29$m/s, respectively; which yields a ratio $c_{\mathrm{P}}/c_{\mathrm{S}} = k_{\mathrm{S}}/k_{\mathrm{P}} \simeq 1.94$.

5.2.2 Error analysis: h-refinement

To investigate the h-convergence of BBFEM, a sequence of five gradually refined mesh grids are considered, with three typical examples being shown in Figure 5.

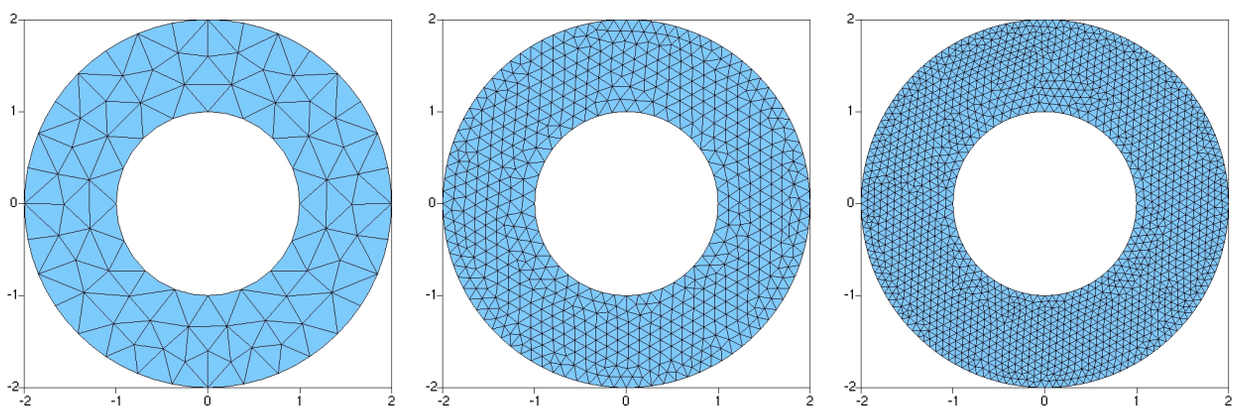

Figure 5: Examples of unstructured mesh grids used for the pulsating cavity problem; from left to right: M_1 ($h = 0.54a$), M_3 ($h = 0.20a$) and M_5 ($h = 0.13a$).

In Figure 6, the relative L^2 error ϵ_2 is plotted against the number τ_{P} of DoF per P wavelength at the frequencies $f = 1.0\times10^4$ Hz, $f = 2.0\times10^4$ Hz and $f = 4.0\times10^4$ Hz, for different values of the polynomial order p in the P wave stress case. Similarly, results of the S wave stress case are shown in

Figure 7, where the relative L^2 error ϵ_2 is now shown versus the number τ_{S} of DoF per S wavelength. As expected, the h-convergence is the faster, the higher polynomial order p is. More precisely, an asymptotically algebraic decay of the L^2 error ϵ_2 scaling as τ_{P}^{-p-1} is clearly seen from Figure 6. The same trend concerning h-convergence is observed for the shear wave problem, especially in the results of Figures 7(a) and 7(b) corresponding to the frequencies $f = 1.0 \times 10^4$ Hz and $f = 2.0 \times 10^4$ Hz, respectively. However, as a consequence of the pollution error, a further increase of the frequency f leads to a pre-asymptotic region of slower convergence involving large values of the mesh size h (see Figure 7(c)). Since the ratio $k_{\mathrm{S}}/k_{\mathrm{P}} \simeq 1.94$, an important difference in error levels, for a given frequency and with the same hp resolution, is observed by comparing the results of Figures 6 and 7. This is due to the fact that the S wavelength is shorter than the P wavelength, and thus a higher resolution is needed to resolve S waves.

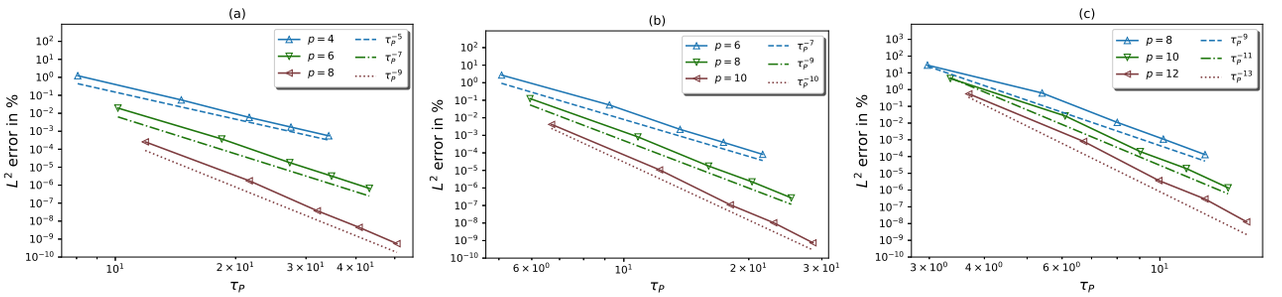

Figure 6: The L^2 error versus τ_{P} (P wave stress); h-refinement for different values of the polynomial order p: (a) $f = 10,000$ Hz, (b) $f = 20,000$ Hz and (c) $f = 40,000$ Hz.

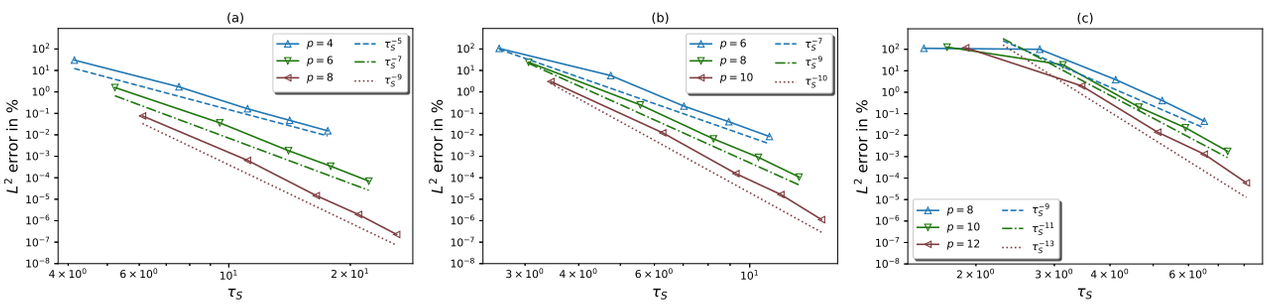

Figure 7: The L^2 error versus τ_{S} (S wave stress); h-refinement for different values of the polynomial order p: (a) $f = 10,000$ Hz, (b) $f = 20,000$ Hz and (c) $f = 40,000$ Hz.

5.2.3 Error analysis: p-refinement

All the numerical experiments in this study are performed on mesh grid M_3, where $h = 0.20a$, with the same frequencies as in the previous subsection. Results of p-convergence analysis are shown in Figures 8(a) and (b), for both P and S wave stress cases. As expected, and since these benchmark tests make use of smooth analytical solutions, an exponential convergence is achieved. However, due to the pollution error, the decay of the L^2 error slows down when the frequency increases, as can be seen from Figure 8 at a frequency $f = 4.0 \times 10^4$ Hz. A pre-asymptotic region of slower convergence with low polynomial orders can be again observed in Figure 8(b), where the S wave is not well resolved.

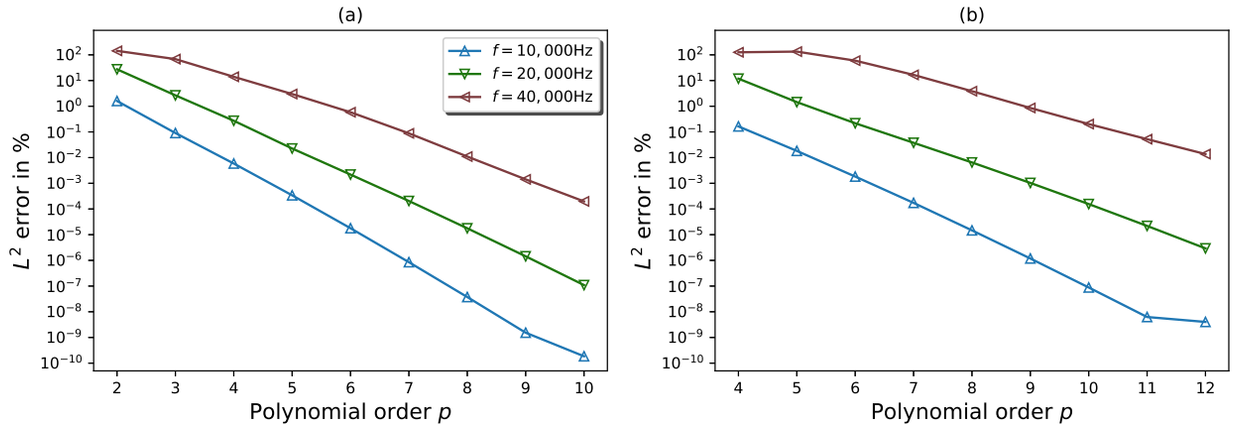

Figure 8: The L^2 error versus the polynomial order for different frequencies; p-refinement with $h = 0.20a$: (a) P wave stress and (b) S wave stress.

When a highly accurate solution is sought, the p (or h) refinement procedure may lead to a slow decay (or even an increase) of the L^2 error as can be observed in Figure 8(b), at $f = 1.0 \times 10^4$ Hz. This is likely due to round-off errors which become very significant as the condition number of the linear system to be solved reaches a certain high level.

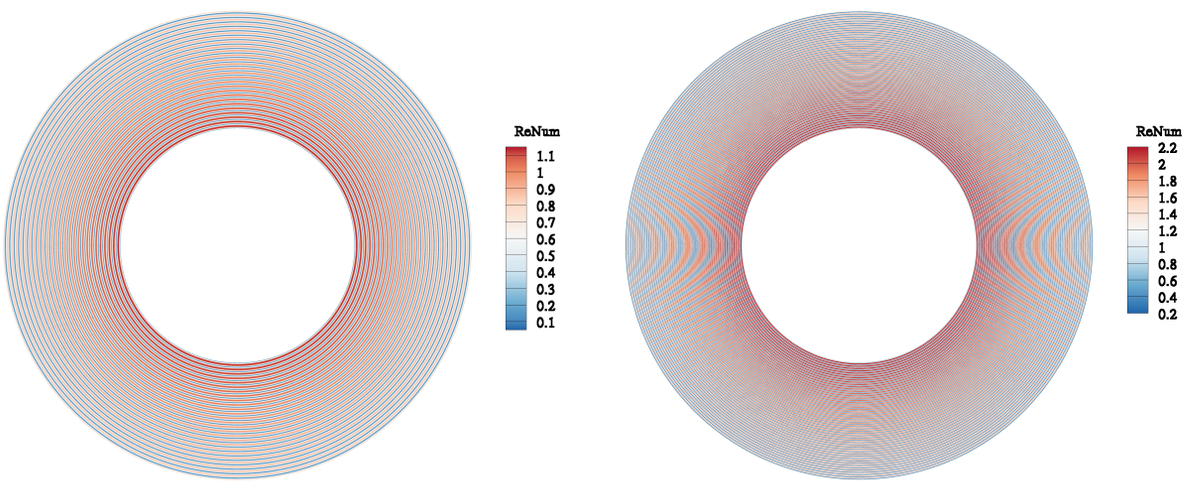

Figure 9: Pulsating cavity; contour plots of $|\mathrm{Re}(\boldsymbol{u}_h)|$ at $f = 8.0 \times 10^4$ Hz, with $h = 0.13a$ and $p = 12$: (left) P wave stress; $\epsilon_2 = 9.16e\text{-}5\%$ and $\tau_\mathrm{P} = 7.87$, and (right) S wave stress; $\epsilon_2 = 0.28\%$ and $\tau_\mathrm{S} = 4.04$.

Figure 9 displays the contour plot of $|\mathrm{Re}(\boldsymbol{u}_h)|$ at $f = 8.0 \times 10^4$ Hz, for both P and S wave stress cases, where computations are carried out on mesh grid M_5 with a polynomial order $p = 12$. As previously mentioned, the notable difference in error levels for both test cases is due to the ratio $\lambda_\mathrm{P}/\lambda_\mathrm{S} \simeq 1.94$ between propagating P and S wavelengths. A good accuracy is achieved in the case of S wave stress (see Figure 9(b)), with only $\tau_\mathrm{S} = 4.04$. It should be noted that elements of mesh grid M_5 in this example may contain up to $h/\lambda_\mathrm{S} \simeq 3.34$ S wavelengths.

5.3 Scattering of elastic plane waves by a rigid cylinder

5.3.1 Description of the problem

As a second benchmark, we deal with the scattering of waves by a rigid body, where an incident plane wave $\boldsymbol{u}^\mathrm{in}$ travelling from left to right along the horizontal direction impinges on an infinite cylinder

of radius a. Even though the first numerical example gives insight into the accuracy of BBFEM, the corresponding analytical solutions do not represent a realistic problem, with a wave field including both propagating and evanescent modes. It should be noted that conventional discretisation schemes may fail to resolve the fast decay of high order evanescent modes. These motivate, accordingly, to investigate wave scattering problems. Here, we use the same model geometry and elastic material parameters as those of the previous benchmark. Two scenarios are considered. The first one concerns P wave scattering, in which the incident displacement field is given by $\boldsymbol{u}^{\text{in}} = \mathrm{i}k_{\text{P}} \exp(\mathrm{i}k_{\text{P}} x_1)\boldsymbol{e}_1$ and the analytical solution of the scattered field is given in the polar coordinate system by [31]:

$$\begin{aligned}
\boldsymbol{u}_r &= \sum_{m=0}^{+\infty} \Big[\varepsilon_m \mathrm{i}^m k_{\text{P}} J'_m(k_{\text{P}} r) + k_{\text{P}} A_m H'_m(k_{\text{P}} r) + m B_m \frac{H_m(k_{\text{S}} r)}{r}\Big] \cos(m\theta) \\
&+ \Big[k_{\text{P}} C_m H'_m(k_{\text{P}} r) - m D_m \frac{H_m(k_{\text{S}} r)}{r}\Big] \sin(m\theta) \\
\boldsymbol{u}_\theta &= \sum_{m=0}^{+\infty} -\Big[\varepsilon_m \mathrm{i}^m m \frac{J_m(k_{\text{P}} r)}{r} + m A_m \frac{H_m(k_{\text{P}} r)}{r} + B_m k_{\text{S}} H'_m(k_{\text{S}} r)\Big] \sin(m\theta) \\
&+ \Big[m C_m \frac{H_m(k_{\text{P}} r)}{r} - D_m k_{\text{S}} H'_m(k_{\text{S}} r)\Big] \cos(m\theta).
\end{aligned} \tag{5.6}$$

The second scenario concerns S wave scattering, where $\boldsymbol{u}^{\text{in}} = -\mathrm{i}k_{\text{S}} \exp(\mathrm{i}k_{\text{S}} x_1)\boldsymbol{e}_2$. The analytical solution of this problem is similarly given by

$$\begin{aligned}
\boldsymbol{u}_r &= \sum_{m=0}^{+\infty} \Big[k_{\text{P}} A_m H'_m(k_{\text{P}} r) + m B_m \frac{H_m(k_{\text{S}} r)}{r}\Big] \cos(m\theta) \\
&+ \Big[-m\varepsilon_{\text{m}} \mathrm{i}^m \frac{J_m(k_{\text{S}} r)}{r} + k_{\text{P}} C_m H'_m(k_{\text{P}} r) - m D_m \frac{H_m(k_{\text{S}} r)}{r}\Big] \sin(m\theta) \\
\boldsymbol{u}_\theta &= \sum_{m=0}^{+\infty} -\Big[m A_m \frac{H_m(k_{\text{P}} r)}{r} + B_m k_{\text{S}} H'_m(k_{\text{S}} r)\Big] \sin(m\theta) \\
&+ \Big[-\varepsilon_m i^m k_{\text{S}} J'_m(k_{\text{S}} r) + m C_m \frac{H_m(k_{\text{P}} r)}{r} - D_m k_{\text{S}} H'_m(k_{\text{S}} r)\Big] \cos(m\theta).
\end{aligned} \tag{5.7}$$

Herein, J_m and H_m are, respectively, the Bessel and Hankel functions of the first kind and order m and the sequence $\{\varepsilon_m\}$ is defined by $\varepsilon_0 = 1$, and $\varepsilon_m = 2$ for all $m \geq 1$. The constants A_m, B_m, C_m and D_m are chosen such that $\boldsymbol{u} = 0$ on the scatterer boundary. In what follows, the above infinite series are truncated to a finite number N_t of terms.

5.3.2 Error analysis: h-refinement

Likewise, we perform h-convergence analysis using the same mesh grids of Figure 5, by taking $N_t \simeq k_{\text{S}} a$. It is noteworthy that the choice of N_t does not affect accuracy, because the truncated analytical solution is enforced by the Robin boundary condition (2.4). This choice involves propagating S wave modes ($m \leqslant k_{\text{S}} a$), propagating ($m \leqslant k_{\text{P}} a$) and evanescent ($k_{\text{P}} a < m \leqslant N_t$) P wave modes, respectively.

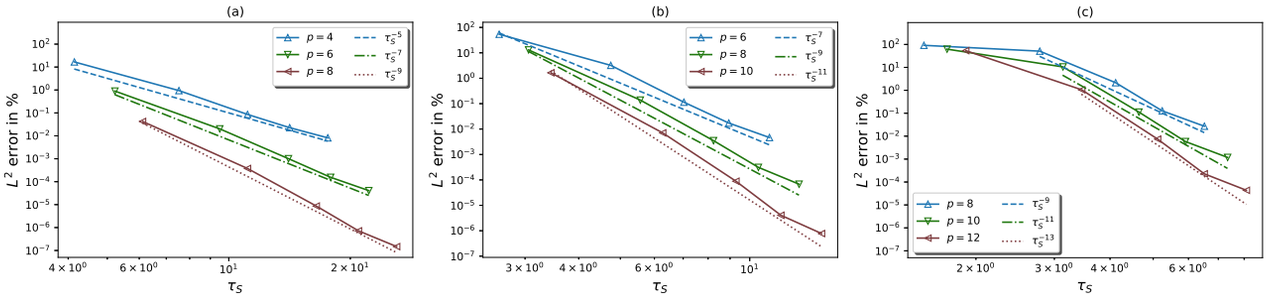

Figure 10: The L^2 error versus τ_S; P wave scattering: h-refinement for different values of the polynomial p: (a) $f = 10,000$ Hz, (a) $f = 20,000$ Hz and (c) $f = 40,000$ Hz.

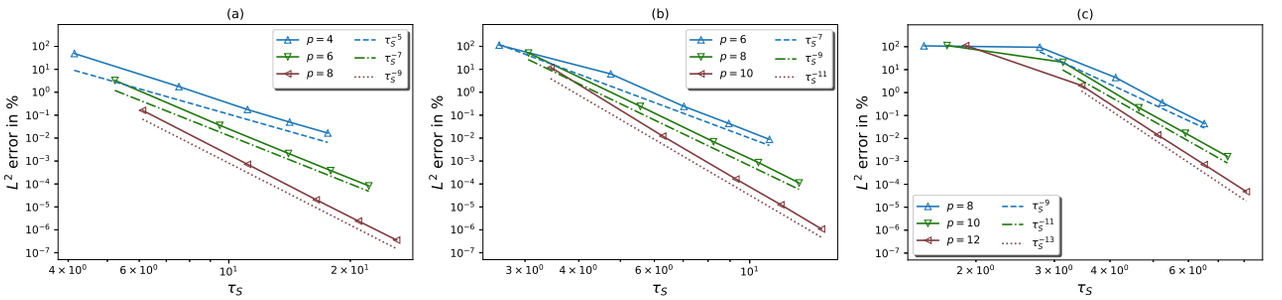

Figure 11: The L^2 error versus τ_S; S wave scattering; h-refinement for different values of the polynomial p: (a) $f = 10,000$ Hz, (a) $f = 20,000$ Hz and (c) $f = 40,000$ Hz.

Results of P wave scattering are shown in Figure 10, with the L^2 error being plotted versus the number τ_S of DoF per S wavelength at $f = 1.0 \times 10^4$ Hz, $f = 2.0 \times 10^4$ Hz and $f = 4.0 \times 10^4$ Hz, for increasing polynomial orders. It should be noted that the analytical solution (5.6) of the P wave scattering problem involves both P and S waves and hence L^2 error is plotted against τ_S. In the same fashion, those of S wave scattering are reported in Figure 11.

Results of Figures 10 and 11 reveal a similar trend in terms of h-convergence behaviour, compared to those of the previous benchmark with a prescribed S stress. In particular, the asymptotically algebraic decay of the L^2 error is well recovered, and pre-asymptotic regions of slower convergence, where the mesh size h is large compared to the S wavelength, are again observed at $f = 40,000$ Hz (see Figures 10(c) and 11(c)).

5.3.3 Error analysis: p-refinement

We now investigate p-convergence analysis. Numerical experiments are performed on mesh grid M_3 shown in Figure 5, at the same frequencies as before. In Figure 12, the L^2 error ϵ_2 is shown versus the polynomial order p for different frequencies and both P and S wave scattering problems. Results of Figure 12 indicate a similar trend in terms of p-convergence compared to those of the p-refinement analysis, carried out previously in the pulsating cavity problem with a prescribed S wave stress. Most importantly, an exponential decay of the L^2 error is again observed from Figures 12(a) and 12(b). Additionally, pre-asymptotic regions of slower convergence with lower polynomial orders are seen as well. Results of Figure 12(a) also show that the L^2 error stagnates at $f = 1.0 \times 10^4$ Hz when high accuracy is sought. This is likely due, as mentioned previously, to round-off errors which are significantly affected when the condition number is large.

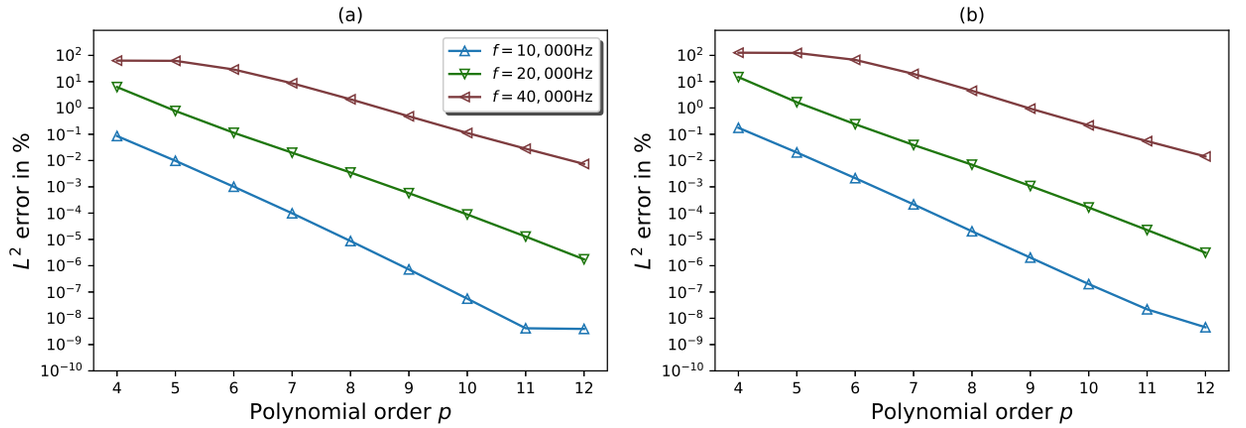

Figure 12: The L^2 error versus the polynomial order p for different frequencies; p-refinement with $h = 0.20a$: (a) P wave scattering; (b) S wave scattering.

Figure 13 displays the contour plot of $|\mathrm{Re}(\boldsymbol{u}_h)|$ at $f = 8.0\times10^4$ Hz, with $N_t \simeq 2k_{\mathrm{S}}a$. Computations been performed, for both P and S wave scattering problems, on mesh grid M_5 with a polynomial order $p = 12$. It is worth mentioning that with the choice $N_t \simeq 2k_{\mathrm{S}}a$, the analytical solution also involves high order evanescent S wave modes ($k_{\mathrm{S}}a \ll m \leqslant 2k_{\mathrm{S}}a$).

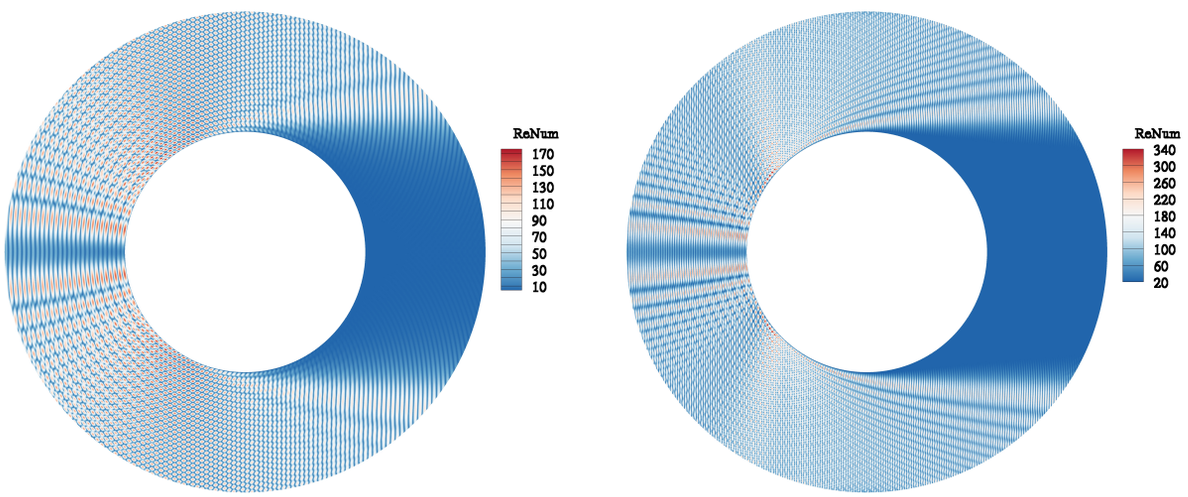

Figure 13: Wave scattering; contour plot of $|\mathrm{Re}(\boldsymbol{u}_h)|$ at $f = 8.0 \times 10^4$ Hz; $N_t \simeq 2k_{\mathrm{S}}a$: (left) P wave scattering and (right) S wave scattering; $\epsilon_2 = 0.21\%$ and τ_{S} =4.04.

Good quality results are obtained with only τ_{S} =4.04 for both P and S wave scattering problems, using mesh grid M_5, where elements may contain up to $h/\lambda_{\mathrm{S}} \simeq 3.34$ S wavelengths.

5.4 Elastic wave transmission

5.4.1 Description of the problem

This last benchmark deals with wave scattering problems in an elastic medium with an interface. It was designed to demonstrate the ability of BBFEM combined with a non uniform p-refinement procedure, in efficiently handling cases of high wave speed contrast between two media, where an accurate representation of the interior interface is mandatory. We analyze the transmission of elastic plane waves through a homogeneous elastic cylinder of radius a, embedded in an infinite homogeneous elastic medium of different material. The geometry of the problem is sketched in Figure 14 (left),

where the outer radius $R = 2a$. The elastic properties of medium Ω_2 are chosen such that $\nu_2 = \nu$, $E_2 = E$ and $\rho_2 = \rho$, where ν, E and ρ are given in Table 1, while those of medium Ω_1 are given by $\nu_1 = \nu$, $E_1 = n^2 E$ and $\rho_1 = \rho$, with $n = 2$ or 4. These yield a ratio $k_{\mathrm{S}}^{(2)}/k_{\mathrm{S}}^{(1)} = n$, where $k_{\mathrm{S}}^{(1)}$ and $k_{\mathrm{S}}^{(2)}$ are the S wavenumbers in the elastic media Ω_1 and Ω_2, respectively.

As before, we consider two scenarios with P and S incident plane waves travelling from left to right in the horizontal direction along the x_1-axis. For the case of P incident plane wave, the analytical solution can be found in [81], while for that of S incident plane wave, it is given in Appendix A. A similar example was dealt with in [28]. All computations are performed on the interface fitted mesh grid depicted in Figure 14 (right), where the geometry of curved elements sharing an edge with the interface Σ is interpolated using the blending map of Gordon and Hall defined in Subsection 4.2.

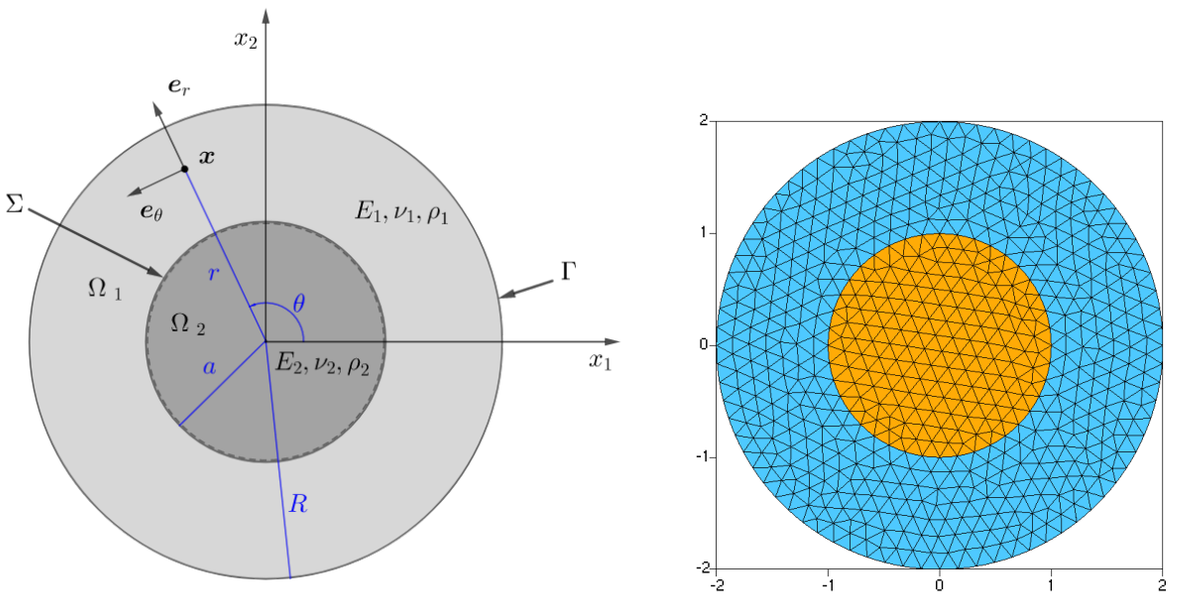

Figure 14: (Left) Schematic diagram defining the parameters of the elastic wave transmission problem; (right) typical interface fitted mesh grid, with $h = 0.22a$.

5.4.2 Non uniform p-refinement

Since the transmission problem occurs in heterogeneous regions with many elastic properties of media, it is useful to vary the polynomial degree in each area. According to the choices made above of the elastic material properties, two ratios are considered: $k_{\mathrm{S}}^{(2)}/k_{\mathrm{S}}^{(1)} = 2$ and $k_{\mathrm{S}}^{(2)}/k_{\mathrm{S}}^{(1)} = 4$, respectively. Let p be the polynomial order chosen to resolve the wave in medium Ω_2, where $k_{\mathrm{S}}^{(2)} > k_{\mathrm{S}}^{(1)}$. Then, we take $p_2 = p$ as the polynomial order for vertex, edge and cell shape functions of elements located in Ω_2. A simple procedure is used in order to choose the polynomial order p_1 in Ω_1:

$$\frac{k_{\mathrm{S}}^{(1)} h_1}{p_1} \backsimeq \frac{1}{\gamma} \frac{k_{\mathrm{S}}^{(2)} h_2}{p_2}, \quad \text{with} \quad \gamma \in \left]1, k_{\mathrm{S}}^{(2)}/k_{\mathrm{S}}^{(1)}\right[, \tag{5.8}$$

where h_i denote the mesh size of region Ω_i for $i = 1, 2$. It is not intended here to provide a sophisticated p-adaptive procedure, but rather to show the applicability of BBFEM with non uniform polynomial order.

In all that follows, we set $\gamma = \frac{1}{2}\left(1 + \frac{k_{\mathrm{S}}^{(2)}}{k_{\mathrm{S}}^{(1)}}\right)$. Formula (5.8) is used to specify the polynomial order p_1 for all the shape functions of elements located in medium Ω_1 not sharing a vertex or edge with the interface Σ, as shown in Figure 15 (left). For those having a vertex or an edge in common with Σ,

the polynomial order of the corresponding cell shape functions is set equal to p_2, and the one of the edge shape functions is obtained by enforcing the minimum order rule for H^1-conforming FEs [73], as illustrated in Figure 15 (right).

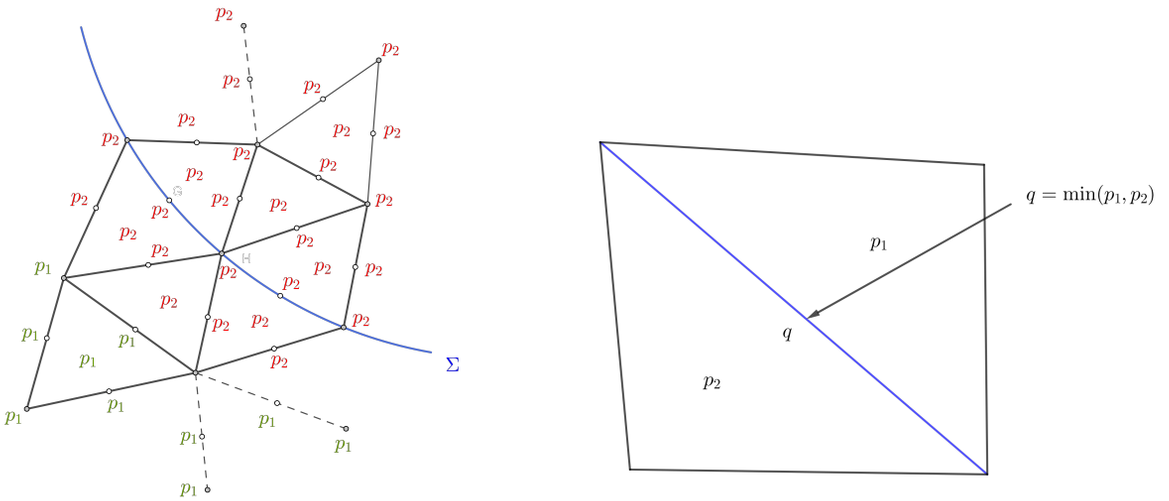

Figure 15: Schematic diagrams showing: (left) the chosen polynomial order for vertex, edge and cell shape functions; (right) minimum order rule.

Table 2 reports the L^2 error ϵ_2 and condition number κ_A obtained using both uniform and non-uniform p-refinement procedures for the same frequencies as before, when the ratio $k_{\mathrm{S}}^{(2)}/k_{\mathrm{S}}^{(1)} = 2$ in the case of S incident plane wave. The total numbers of DoF n_{dof} and non-zero entries nnz in the condensed global matrix, and CPU time in seconds spent in solving the condensed linear system, are also reported. Results of Table 2 indicate that the non uniform p-refinement enables us to achieve a reduction by up to 18%, 30% and 34% in the total numbers of DoF and non-zero entries, and CPU time, respectively, while keeping comparable accuracy and condition number. This procedure may also help in improving the L^2 error, especially for highly accurate solutions, as can be seen from Table 2 when $f = 1.0 \times 10^4$ Hz and $p = 12$.

	Uniform p-refinement						Non uniform p-refinement					
f	p	n_{dof}	nnz	CPU	ϵ_2[%]	κ_A	(p_1, p_2)	n_{dof}	nnz	CPU	ϵ_2[%]	κ_A
	4	12,206	262,589	0.35	0.25	0.92e+3	(3,4)	9,702	180,369	0.28	0.33	0.87e+3
	6	19,498	610,779	0.95	2.35e-3	0.18e+4	(5,6)	16,994	479,695	0.76	2.46e-3	0.18e+4
10 kHz	8	26,790	1,102,377	2.05	2.10e-5	0.10e+5	(6,8)	21,782	766,593	1.35	5.91e-5	0.10e+5
	10	34,082	1,737,383	3.49	4.81e-7	0.10e+6	(8,10)	29,074	1,303,871	2.67	4.30e-7	0.10e+6
	12	41,374	2,515,797	6.25	4.22e-7	0.12e+7	(9,12)	33,862	1,755,105	4.14	3.68e-8	0.11e+7
	4	12,206	262,589	0.38	4.45e+1	0.10e+4	(3,4)	9,702	180,369	0.27	48.25	0.96e+3
	6	19,498	610,779	0.99	0.43	0.19e+4	(5,6)	16,994	479,695	0.74	0.43	0.19e+4
20 kHz	8	26,790	1,102,377	2.09	8.82e-3	0.77e+4	(6,8)	21,782	766,593	1.33	9.42e-3	0.77e+4
	10	34,082	1,737,383	3.65	2.21e-4	0.80e+5	(8,10)	29,074	1,303,871	2.56	2.25e-4	0.80e+5
	12	41,374	2,515,797	5.41	4.33e-6	0.97e+6	(9,12)	33,862	1,755,105	3.90	5.99e-6	0.97e+6
	8	26,790	1,102,377	2.28	61.01	0.49e+6	(6,8)	21,782	766,593	1.36	60.49	0.48e+6
	10	34,082	1,737,383	3.80	1.02	0.19e+7	(8,10)	29,074	1,303,871	2.68	1.02	0.19e+7
40 kHz	12	41,374	2,515,797	6.43	2.03e-2	0.26e+8	(9,12)	33,862	1,755,105	4.11	2.04e-2	0.26e+8
	14	48,666	3,437,619	9.24	1.08e-3	0.54e+9	(11,14)	41,154	2,530,335	6.80	1.08e-3	0.54e+9

Table 2: Uniform p-refinement vs. non-uniform p-refinement results: S incident plane wave; $k_{\mathrm{S}}^{(2)}/k_{\mathrm{S}}^{(1)} = 2$.

In the same fashion, results with a ratio $k_{\mathrm{S}}^{(2)}/k_{\mathrm{S}}^{(1)} = 4$ are reported in Table 3. When $f = 1.0 \times 10^4$ Hz, the non-uniform p-refinement procedure provides an accuracy which is one order of magnitude higher for some moderate values of the polynomial order p. To avoid this drawback, we can increase the parameter γ in Formula (5.8). But this comes at the price of increasing the total numbers of DoF and non-zero entries as well. However, as the polynomial order increases a significant improvement in accuracy for the same frequency ($f = 1.0 \times 10^4$ Hz) is seen with a reduction by up to 24%, 38% and 42% in the total numbers of DoF and non-zero entries, and CPU time, respectively. By increasing now the frequency, similar reductions in the total numbers of DoF and non-zero entries are achieved, with comparable accuracy and condition number, as can be observed in Table 3.

	Uniform p-refinement						Non uniform p-refinement					
f	p	n_{dof}	nnz	CPU	ϵ_2[%]	κ_A	(p_1, p_2)	n_{dof}	nnz	CPU	ϵ_2[%]	κ_A
	4	12,206	262,589	0.36	5.75	0.99e+4	(3,4)	9,702	180,369	0.25	6.47	0.95e+4
	6	19,498	610,779	1.00	3.07e-3	0.14e+5	(4,6)	14490	372723	0.58	1.19e-2	0.11e+5
10 kHz	8	26,790	1,102,377	2.28	2.07e-5	0.25e+5	(5,8)	19,278	634,869	1.09	1.85e-4	0.18e+5
	10	34,082	1,737,383	3.48	1.32e-6	0.10e+6	(7,10)	26,570	1,123,283	2.12	1.05e-6	0.10e+6
	12	41,374	2,515,797	5.21	5.50e-6	0.10e+7	(8,12)	31,358	1,549,765	3.03	9.63e-8	0.10e+7
	4	12,206	262,589	0.36	97.25	0.24e+4	(3,4)	9,702	180,369	0.25	97.28	0.20e+4
	6	19,498	610,779	0.97	0.75	0.25e+4	(4,6)	14,490	372723	0.56	0.75	0.25e+4
20 kHz	8	26,790	1,102,377	2.04	1.07e-2	0.61e+4	(5,8)	19,278	634,869	1.10	1.07e-2	0.59e+4
	10	34,082	1,737,383	3.50	2.92e-4	0.57e+5	(7,10)	26,570	1,123,283	2.12	2.92e-4	0.57e+5
	12	41,374	2,515,797	5.65	6.38e-6	0.73e+6	(8,12)	31,358	1,549,765	3.06	6.30e-6	0.73e+6
	8	26,790	1,102,377	2.07	72.77	0.55e+6	(5,8)	19,278	634,869	1.34	72.66	0.55e+6
	10	34,082	1,737,383	3.61	2.27	0.58e+6	(7,10)	26,570	1,123,283	2.16	2.27	0.58e+6
40 kHz	12	41,374	2,515,797	6.40	5.51e-2	0.10e+8	(8,12)	31,358	1,549,765	3.16	5.51e-2	0.10e+8
	14	48,666	3,437,619	8.42	3.11e-3	0.19e+9	(9,14)	36,146	2,046,039	4.91	3.52e-3	0.19e+9

Table 3: Uniform p-refinement vs. non-uniform p-refinement results; elastic wave transmission problems: S incident plane wave; $k_{\mathrm{S}}^{(2)}/k_{\mathrm{S}}^{(1)} = 4$.

Figure 16 displays the contour plot of $|\mathrm{Re}(\boldsymbol{u}_h)|$ at $f = 4.0 \times 10^4$ Hz, using a non uniform polynomial order and $N_t \simeq k_{\mathrm{S}}^{(2)} a$, for both P and S elastic wave transmission problems.

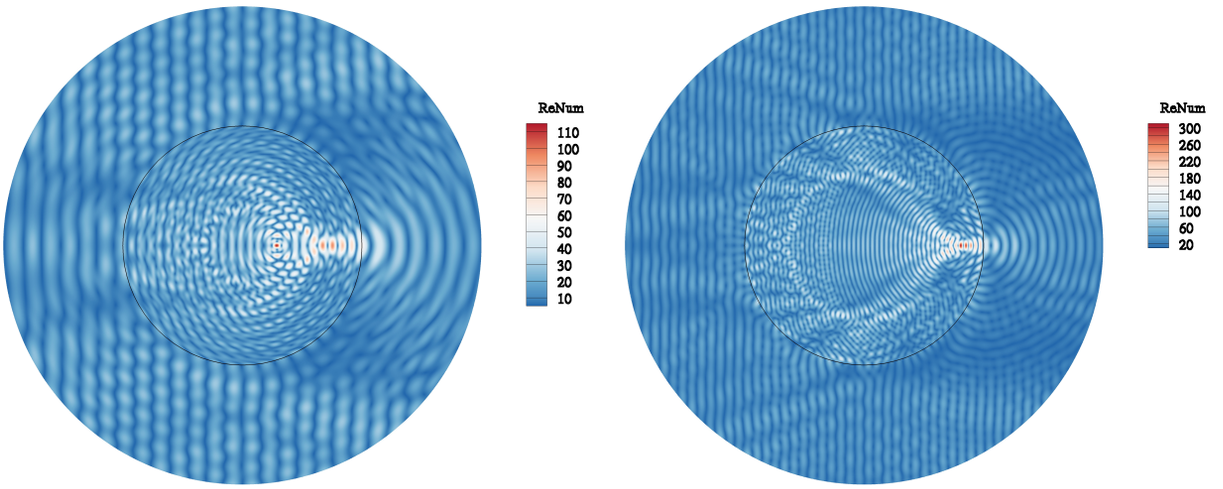

Figure 16: Contour plot of $|\mathrm{Re}(\boldsymbol{u}_h)|$ at $f = 4.0 \times 10^4$ Hz, with $N_t \simeq k_{\mathrm{S}}^{(2)} a$, $(p_1, p_2) = (9, 12)$, $\tau_{\mathrm{S}} = 6.10$ and $k_{\mathrm{S}}^{(2)}/k_{\mathrm{S}}^{(1)} = 2$; elastic wave transmission problems: (left) P incident wave; $\epsilon_2 = 0.01\%$, and (right) S incident wave; $\epsilon_2 = 0.02\%$.

Good accuracies are achieved with $\tau_{\mathrm{S}} = 6.10$, where elements in the computational mesh grid may contain up $h_2/\lambda_{\mathrm{S}}^{(2)} \simeq 2.8$ S wavelengths.

6 Conclusions

In this paper, BBFEM has been extended to efficiently solve time-harmonic elastic wave problems, using unstructured triangular mesh grids. Key aspects of the method rely on the use of analytical rules to set up the local FE matrices for affine elements, while the tensorial construction of Bernstein polynomials amenable to sum factorisation is exploited for curved elements to speed up the assembly process. These yield a notable saving in terms of computational cost and hence afford high order computations. In addition, static condensation is applied at the element level to efficiently solve the resulting condensed linear system.

The performance of BBFEM has been assessed, in terms of accuracy and memory requirements, on various benchmark tests. Results of h and p convergence analysis show that the proposed method enables us the recovery of the expected exponential and algebraic convergence rates. Furthermore, the p version of BBFEM has proven more effective in mitigating the pollution effect and accurately resolving high order evanescent P and S wave modes, involved in the elastic wave scattering problems. Besides, the applicability of BBFEM with a variable polynomial order, based on a simple *a priori* indicator has been demonstrated by considering elastic wave transmission problems, with high wave speed contrast. The results show the benefit of the non uniform p-refinement procedure in improving accuracy and efficiency, and how the high geometric flexibility of BBFEM in conjunction with a blending map method makes it possible to simulate computational domains including a curved interface with very high accuracy.

The computational efficiency of the Bernstein basis functions can be fully exploited by extending the optimal assembly algorithm proposed in [63]. This is of a relevant importance, especially when tackling wave problems with variable coefficients and three-dimensional space computations. Since the overhead for performing numerical integration on curved elements is negligible, given that such elements are a small percent of all the mesh grid elements in the benchmarks dealt with in this work, a nearly optimal procedure has been adopted for ease of implementation.

This present work focuses solely on the computation cost of assembly. A thorough study, including

the computation costs of the solution processing and static condensation, is crucial for providing a clear insight on the overall efficiency of BBFEM, for different *hp* discretisations and at a predefined level of accuracy. The optimal choice of the element order minimizing the computational effort is, however, not trivial as it heavily depends on the wavenumber [60].

A future work should account for *hp*-adaptivity to further enhance computational efficiency and take full benefit of BBFEM. Other possible research directions include the use of a robust preconditioned iterative solver to reduce memory requirements. Building on these encouraging results, it is also planned to extend the method to 3D elastic wave computations.

A Analytical solution of the transmission problem: incident S plane wave

The elastic constants of the medium $\Omega_1 = (a < r < R)$ and its density are denoted respectively by ν_1, E_1 and ρ_1, and those of the elastic cylinder $\Omega_2 = (r < a)$ are denoted by ν_2, E_2 and ρ_2. Assume ν_1, E_1 and ρ_1, differ from ν_2, E_2 and ρ_2. Then the incident S plane wave

$$\psi_{\text{in}} = \exp(\mathrm{i}k_{\text{S}}^{(1)}x_1) \tag{A.1}$$

will travel through the elastic medium until it hits the elastic cylinder, then it will be reflected from the boundary of the cylinder resulting in a wave that propagates outward. While the refracted part of the incident waves will be confined in the cylinder and generates a standing wave. Therefore, the analytical solution for this problem consists of the total wave outside the cylinder denoted by $\boldsymbol{u}_1$, which is a superposition of the incident and the reflected waves, and the total wave inside the cylinder denoted by $\boldsymbol{u}_2$ which is a refracted wave. Thus, we have

$$\begin{cases} \boldsymbol{u}_1 = \boldsymbol{u}_{\text{in}} + \boldsymbol{u}_R \\ \boldsymbol{u}_2 = \boldsymbol{u}_F, \end{cases} \tag{A.2}$$

where $\boldsymbol{u}_{\text{in}}$ is derived from the potential ψ_{in}, i.e.

$$\boldsymbol{u}_{\text{in}} = \boldsymbol{\nabla} \times \psi_{\text{in}}. \tag{A.3}$$

The reflected displacement $\boldsymbol{u}_R$ is the solution of the following Navier equation:

$$\begin{aligned} -\rho\omega^2\boldsymbol{u}_R - \boldsymbol{\nabla}\cdot\boldsymbol{\sigma}(\boldsymbol{u}_R) = 0 \quad &\text{in} \quad \Omega_1 \\ \boldsymbol{u}_R + \boldsymbol{u}_{\text{in}} = 0 \quad &\text{on} \quad \Sigma = (r = a). \end{aligned} \tag{A.4}$$

The refracted displacement $\boldsymbol{u}_F$ is the solution of the following Navier equation:

$$\begin{aligned} -\rho\omega^2\boldsymbol{u}_F - \boldsymbol{\nabla}\cdot\boldsymbol{\sigma}(\boldsymbol{u}_F) = 0 \quad &\text{in} \quad \Omega_2 \\ \boldsymbol{u}_F = 0 \quad &\text{on} \quad \Sigma. \end{aligned} \tag{A.5}$$

By using the Helmholtz decomposition theorem, the displacements $\boldsymbol{u}_R$ and $\boldsymbol{u}_F$ can be written in terms of the potentials (φ_R, ψ_R) and (φ_F, ψ_F) as follows:

$$\begin{cases} \boldsymbol{u}_R = \boldsymbol{\nabla}\varphi_R + \boldsymbol{\nabla}\times\psi_R \\ \boldsymbol{u}_F = \boldsymbol{\nabla}\varphi_F + \boldsymbol{\nabla}\times\psi_F, \end{cases} \tag{A.6}$$

where the curl operator $\boldsymbol{\nabla}\times$ is defined for a given scalar field ϕ by $\boldsymbol{\nabla}\times\phi = (\partial_2\phi, -\partial_1\phi)^\top$ and $\varphi_R, \psi_R, \varphi_F$ and ψ_F are solutions for the following Helmholtz equations:

$$\begin{aligned} &-k_{\text{P}}^2\varphi_R - \Delta\varphi_R = 0, \quad -k_{\text{S}}^2\psi_R - \Delta\psi_R = 0 \\ &-k_{\text{P}}^2\varphi_F - \Delta\varphi_F = 0, \quad -k_{\text{S}}^2\psi_F - \Delta\psi_F = 0. \end{aligned} \tag{A.7}$$

The displacement potentials for the reflected waves are:

$$\varphi_R = \sum_{m=0}^{+\infty} A_m H_m^{(1)}(k_{\mathrm{P}}^{(1)} r)\sin(m\theta), \quad \psi_R = \sum_{m=0}^{+\infty} B_m H_m^{(1)}(k_{\mathrm{S}}^{(1)} r)\cos(m\theta), \tag{A.8}$$

while the displacement potentials for the refracted standing waves inside the circular cylinder can be represented as:

$$\varphi_F = \sum_{m=0}^{+\infty} C_m J_m(k_{\mathrm{P}}^{(2)} r)\sin(m\theta), \quad \psi_F = \sum_{m=0}^{+\infty} D_m J_m(k_{\mathrm{S}}^{(2)} r)\cos(m\theta). \tag{A.9}$$

The Jacobi-Anger expansion for the incident potential ψ_{in} reads as

$$\psi_{\mathrm{in}} = \sum_{m=0}^{+\infty} \varepsilon_m i^m J_m(k_{\mathrm{S}}^{(1)} r)\cos(m\theta), \tag{A.10}$$

where the sequence $\{\varepsilon_m\}$ is defined by $\varepsilon_0 = 1$, and $\varepsilon_m = 2$ for all $m \geq 1$. Thus, by using (A.3) and (A.6), we have:

$$\begin{cases} \boldsymbol{u}_1 = \boldsymbol{\nabla} \times \psi_{\mathrm{in}} + \boldsymbol{\nabla}\varphi_R + \boldsymbol{\nabla} \times \psi_R \\ \boldsymbol{u}_2 = \boldsymbol{\nabla}\varphi_F + \boldsymbol{\nabla} \times \psi_F. \end{cases} \tag{A.11}$$

Finally, the analytical solution for this problem can be written in the polar coordinate system $(\mathbf{e}_r, \mathbf{e}_\theta)$ as

$$\begin{cases} \boldsymbol{u}_1 = \boldsymbol{u}_{1r}\mathbf{e}_r + \boldsymbol{u}_{1\theta}\mathbf{e}_\theta \\ \boldsymbol{u}_2 = \boldsymbol{u}_{2r}\mathbf{e}_r + \boldsymbol{u}_{2\theta}\mathbf{e}_\theta, \end{cases} \tag{A.12}$$

where

$$\begin{aligned} \boldsymbol{u}_{1r} &= \sum_{m=0}^{+\infty} \Big[-m\varepsilon_m i^m \frac{J_m(k_{\mathrm{S}}^{(1)} r)}{r} + A_m k_{\mathrm{P}}^{(1)} H_m'(k_{\mathrm{P}}^{(1)} r) - mB_m \frac{H_m(k_{\mathrm{S}}^{(1)} r)}{r} \Big] \sin(m\theta) \\ \boldsymbol{u}_{1\theta} &= \sum_{m=0}^{+\infty} \Big[-\varepsilon_m i^m k_{\mathrm{S}}^{(1)} J_m'(k_{\mathrm{S}}^{(1)} r) + mA_m \frac{H_m(k_{\mathrm{P}}^{(1)} r)}{r} - B_m k_{\mathrm{S}}^{(1)} H_m'(k_{\mathrm{S}}^{(1)} r) \Big] \cos(m\theta) \\ \boldsymbol{u}_{2r} &= \sum_{m=0}^{+\infty} \Big[C_m k_{\mathrm{P}}^{(2)} J_m'(k_{\mathrm{P}}^{(2)} r) - mD_m \frac{J_m(k_{\mathrm{S}}^{(2)} r)}{r} \Big] \sin(m\theta) \\ \boldsymbol{u}_{2\theta} &= \sum_{m=0}^{+\infty} \Big[mC_m \frac{J_m(k_{\mathrm{P}}^{(2)} r)}{r} - D_m k_{\mathrm{S}}^{(2)} J_m'(k_{\mathrm{S}}^{(2)} r) \Big] \cos(m\theta), \end{aligned} \tag{A.13}$$

and the constants A_m, B_m, C_m and D_m in equations (A.13) are to be determined by enforcing the transmission boundary conditions :

$$\boldsymbol{u}_1 = \boldsymbol{u}_2 \quad \text{and} \quad \boldsymbol{\sigma}(\boldsymbol{u}_1)\boldsymbol{n}_1 + \boldsymbol{\sigma}(\boldsymbol{u}_2)\boldsymbol{n}_2 = 0 \quad \text{on} \quad \Sigma.$$

References

[1] F. Ihlenburg and I. Babuška. Dispersion analysis and error estimation of Galerkin finite element methods for the Helmholtz equation. *Int. J. Numer. Methods Eng.* 38 (1995): 3745–3774.

[2] F. Ihlenburg and I. Babuška. Finite-element solution of the Helmholtz-equation with high wavenumber. Part I: the *h*-version of the FEM. *Computers and Mathematics with Applications.* 30 (1995): 9–37.

[3] F. Ihlenburg and I. Babuška. Finite element solution of the Helmholtz equation with high wavenumber. Part II: The *hp*-version of the FEM. *SIAM Journal on Numerical Analysis.* 34 (1997): 315–358.

[4] I. Babuška and S. A. Sauter. Is the pollution effect of the FEM avoidable for the Helmholtz equation considering high wave numbers?. *SIAM Review.* 42(3) (2000): 451–484.

[5] J. M. Melenk and I. Babuška. The partition of unity finite element method: basic theory and applications. *Computer Methods in Applied Mechanics and Engineering.* 139 (1996): 289–314.

[6] I. Babuška and J. M. Melenk. The partition of unity method. *International Journal for Numerical Methods in Engineering.* 40 (1997): 727–758.

[7] O. Laghrouche and P. Bettess. Short wave modelling using special finite elements. *Journal of Computational Acoustics.* 8(1) (2000): 189–210.

[8] P. Ortiz and E. Sanchez. An improved partition of unity finite element model for diffraction problems. *International Journal for Numerical Methods in Engineering.* 50 (2001): 2727–2740.

[9] O. Laghrouche, P. Bettess and R. J. Astley. Modelling of short wave diffraction problems using approximating systems of plane waves. *International Journal for Numerical Methods in Engineering.* 54 (2002): 1501–1533.

[10] E. Perrey-Debain, O. Laghrouche, P. Bettess and J. Trevelyan. Plane wave basis finite elements and boundary elements for three dimensional wave scattering. *Philosophical Transactions of the Royal Society A.* 362 (2004): 561–577.

[11] O. Laghrouche, P. Bettess, E. Perrey-Debain and J. Trevelyan. Wave interpolation finite elements for Helmholtz problems with jumps in the wave speed. *Computer Methods in Applied Mechanics and Engineering.* 194 (2005): 367–381.

[12] O. Laghrouche, P. Bettess, E. Perrey-Debain and J. Trevelyan. Plane wave basis for wave scattering in three dimensions. *Communications in Numerical Methods in Engineering.* 19 (2003): 715–723.

[13] O. Laghrouche and M. Shadi Mohamed. Locally enriched finite elements for the Helmholtz equation in two dimensions. *Computers & structures.* 88 (23-24) (2010): 1469-1473.

[14] M. Shadi Mohamed, O. Laghrouche and A. El Kacimi. Some numerical aspects of the PUFEM for efficient solution of 2D Helmholtz problems. *Computers & structures.* 88 (23-24) (2010): 1484-1491.

[15] T. Strouboulis, I. Babuška and R. Hidajat. The generalized finite element method for Helmholtz equation: theory, computation, and open problems. *Computer Methods in Applied Mechanics and Engineering.* 195 (2006): 4711–4731.

[16] T. Strouboulis, R. Hidajat and I. Babuška. The generalized finite element method for Helmholtz equation. Part II: Effect of choice of handbook functions, error due to absorbing boundary conditions and its assessment. *Computer Methods in Applied Mechanics and Engineering.* 197 (2008): 364–380.

[17] O. Cessenat and B. Després. Application of an ultra weak variational formulation of elliptic PDEs to the two-dimensional Helmholtz problem. *SIAM Journal on Numerical Analysis.* 35(1) (1998): 255–299.

[18] T. Huttunen, P. Monk and J. P. Kaipio. Computation aspects of the ultra weak variational formulation. *Journal of Computational Physics.* 182 (2002): 27–46.

[19] O. Cessenat and B. Després. Using plane waves as base functions for solving time harmonic equations with the ultra weak variational formulation. *Journal of Computational Acoustics.* 11(22) (2003): 227–238.

[20] P. Monk and D. Q. Wang. A least-squares method for the Helmholtz equation. *Computer Methods in Applied Mechanics and Engineering.* 175 (1999): 121–136.

[21] C. Farhat, I. Harari and L. Franca. The discontinuous enrichment method. *Computer Methods in Applied Mechanics and Engineering.* 190 (2001): 6455–6479.

[22] C. Farhat, I. Harari and U. Hetmanuk. A discontinuous Galerkin method with Lagrange multipliers for the solution of Helmholtz problems in the mid-frequency regime. *Computer Methods in Applied Mechanics and Engineering.* 192 (2003): 1389–1419.

[23] G. Gabard. Discontinuous Galerkin methods with plane waves for time-harmonic problems. *Journal of Computational Physics.* 225 (2) (2007): 1961–1984.

[24] R. Hiptmair, A. Moiola and I. Perugia. Plane wave discontinuous Galerkin methods for the 2D Helmholtz equation: analysis of the p-version. *SIAM Journal on Numerical Analysis* 49 (1) (2011): 264–284.

[25] C. J. Gittelson and R. Hiptmair. Dispersion analysis of plane wave discontinuous Galerkin methods. *International Journal for Numerical Methods in Engineering* 98 (5) (2014): 313–323.

[26] G. Gabard, P. Gamallo and T. Huttunen. A comparison of wavebased discontinuous Galerkin, ultraweak and leastsquare methods for wave problems. *International Journal for Numerical Methods in Engineering* 85 (3) (2011): 380–402.

[27] E. Perrey-Debain, J. Trevelyan and P. Bettess. P-wave and S-wave decomposition in boundary integral equation for plane elastodynamic problems. *Communications in Numerical Methods in Engineering.* 19 (2003): 945–958.

[28] T. Huttunen, P. Monk, F. Collino and J. P. Kaipio. The Ultra-Weak Variational Formulation for Elastic Wave Problems. *SIAM Journal on Scientific Computing.* 25(5) (2004): 1717–1742.

[29] T. Luostari, T. Huttunen and P. Monk. The Ultra-Weak Variational Formulation for 3D Elastic Wave Problems. *Proceedings of 20th International Congress on Acoustics ICA.* (2010): 23–27.

[30] L. Zhang, R. Tezaur and C. Farhat. The discontinuous enrichment method for elastic wave propagation in the medium-frequency regime. *International Journal for Numerical Methods in Engineering.* 66(13) (2006): 2086–2114.

[31] A. El Kacimi and O. Laghrouche. Numerical modelling of elastic wave scattering in frequency domain by the partition of unity finite element method. *International Journal for Numerical Methods in Engineering.* 77(12) (2009): 1646–1669.

[32] A. El Kacimi and O. Laghrouche. Numerical analysis of two plane wave finite element schemes based on the partition of unity method for elastic wave scattering. *Computers and Structures.* 88(23–24) (2010): 1492–1497.

[33] A. El Kacimi and O. Laghrouche. Improvement of PUFEM for the numerical solution of high-frequency elastic wave scattering on unstructured triangular mesh grids. *International Journal for Numerical Methods in Engineering.* 84(3) (2010): 330–350.

[34] A. El Kacimi and O. Laghrouche. Wavelet based ILU preconditioners for the numerical solution by PUFEM of high frequency elastic wave scattering. *Journal of Computational Physics.* 230(8) (2011): 3119–3134.

[35] O. Laghrouche, A. El Kacimi and J. Trevelyan. Extension of the PUFEM to elastic wave propagation in layered media. *Journal of Computational Acoustics.* 20(2) (2012): 1240006.

[36] S. M. Mahmood, O. Laghrouche, J. Trevelyan and A. El Kacimi. Implementation and computational aspects of a 3D elastic wave modelling by PUFEM. *Applied Mathematical Modelling.* 49 (2017): 568–586.

[37] L. Yuan and Y. Liu. A Trefftz-discontinuous Galerkin method for time-harmonic elastic wave problems. *Computational and Applied Mathematics.* 38(3) (2019): 1–29.

[38] M. Ainsworth and H. A. Wajid. Dispersive and dissipative behavior of the spectral element method. *SIAM Journal Numerical Analysis.* 47 (2009): 3910–3937.

[39] K. Christodoulou, O. Laghrouche, M. Shadi Mohamed and J. Trevelyan. High-order finite elements for the solution of Helmholtz problems. *Computers & Structures.* 191 (2017): 129–139.

[40] S. Petersen, D. Dreyer and V. O. Estorff. Assessment of finite and spectral element shape functions for efficient iterative simulations of interior acoustics. *Computer Methods in Applied Mechanics and Engineering.* 195(44–47) (2006): 6463–6478.

[41] A. Lieu, G. Gabard and H. Bériot. A comparison of high-order polynomial and wave-based methods for Helmholtz problems. *Journal of Computational Physics.* 321 (2016): 105–125.

[42] A. El Kacimi, O. Laghrouche, M. Shadi Mohamed and J. Trevelyan. Bernstein-Bézier based finite elements for efficient solution of short wave problems. *Computer Methods in Applied Mechanics and Engineering.* 343 (2019): 166–185.

[43] S. Giani. High-order/*hp*-adaptive discontinuous Galerkin finite element methods for acoustic problems. *Computing.* 95 (1) (2013): 215–234.

[44] P. F. Antonietti and I. Mazzieri. High-order discontinuous Galerkin methods for the elastodynamics equation on polygonal and polyhedral meshes. *Computer Methods in Applied Mechanics and Engineering.* 342 (2018): 414–437.

[45] T. J. R. Hughes, J. A. Cottrell and Y. Bazilevs. Isogeometric analysis: Cad, finite elements, nurbs, exact geometry and mesh refinement. *Computer Methods in Applied Mechanics and Engineering.* 194(39–41) (2005): 4135–4195.

[46] H. Wu, W. Ye and W. Jiang. Isogeometric finite element analysis of interior acoustic problems. *Applied Acoustics.* 100 (2015): 63–73.

[47] L. Coox, E. Deckers, D. Vandepitte and W. Desmet. A performance study of NURBS-based isogeometric analysis for interior two-dimensional time-harmonic acoustics. *Computer Methods in Applied Mechanics and Engineering.* 305 (2016): 441–467.

[48] T. Khajah, X. Antoine and S. P. Bordas. B-Spline FEM for Time-Harmonic Acoustic Scatteringand Propagation. *Journal of Theoretical and Computational Acoustic.* 27(3) (2019): 1850059.

[49] G. C. Diwan and M. Shadi Mohamed. Pollution studies for high order isogeometric analysis and finite element for acoustic problems. *Computer Methods in Applied Mechanics and Engineering.* 350 (2019): 701–718.

[50] C. Willberg, S. Duczek, J.M.V. Perez, D. Schmicker and U. Gabbert. Comparison of different higher order finite element schemes for the simulation of lamb waves. *Computer Methods in Applied Mechanics and Engineering.* 241 (2012): 246–261.

[51] A. Idesman, D. Phama, J.R. Foley and M.Schmidt. Accurate solutions of wave propagation problems under impact loading by the standard, spectral and isogeometric high-order finite elements. Comparative study of accuracy of different space-discretization techniques. *Finite Elements in Analysis and Design.* 88 (2014): 67-89.

[52] L. Dedè, C. Jäggli and A. Quarteroni. Isogeometric numerical dispersion analysis for two-dimensional elastic wave propagation. *Computer Methods in Applied Mechanics and Engineering.* 284 (2015): 320–348.

[53] L. P. Antolin, A. Buffa, F. Calabrò, M. Martinelli and G. Sangalli. Efficient matrix computation for tensor-product isogeometric analysis: The use ofsum factorization. *Computer Methods in Applied Mechanics and Engineering.* 285 (2015): 817–828.

[54] A. Buffa, G. Sangalli and R. Vázquez. Isogeometric analysis in electromagnetics: B-splines approximation. *Computer Methods in Applied Mechanics and Engineering.* 199 (2015): 1143–1152.

[55] R. Vázquez and A. Buffa. Isogeometric analysis for electromagnetic problems. *IEEE Transactions on Magnetics.* 46(8) (2010): 3305–3308.

[56] A. Ratnani and E. Sonnendrücker. An arbitrary high-order spline finite element solver for the time domain Maxwell equations. *Journal of Scientific Computing.* 51(1) (2012): 87–106.

[57] M. J. Peake, J. Trevelyan, and G. Coates. Extended isogeometric boundary element method (XIBEM) for two-dimensional Helmholtz problems. *Computer Methods in Applied Mechanics and Engineering.* 259 (2013): 93–102.

[58] M. J. Peake, J. Trevelyan, and G. Coates. Extended isogeometric boundary element method (XIBEM) for three-dimensional medium-wave acoustic scattering problems. *Computer Methods in Applied Mechanics and Engineering.* 284 (2015): 762–780.

[59] T. Ayala, J. Videla, C. Anitescu, and E. Atroshchenko. Enriched Isogeometric Collocation for two-dimensionaltime-harmonic acoustics. *Computer Methods in Applied Mechanics and Engineering.* 365 (2020): 113033.

[60] J.C. Brigham, W. Aquino, M.A. Aguilo, and P.J. Diamessis. A spectral finite element approach to modeling soft solids excited with high-frequency harmonic loads. *Computer methods in applied mechanics and engineering.* 200, 5-8 (2011): 692–698.

[61] S. A. Orszag. Spectral methods for problems in complex geometries. *Journal of Computational Physics.* 37 (1980): 70–92.

[62] G. E. Karniadakis and S. J. Sherwin. Spectral/*hp* element methods for computational fluid dynamics. Numerical Mathematics and Scientific Computation. *Oxford University Press, New York,* 2005.

[63] M. Ainsworth, G. Andriamaro and O. Davydov. Bernstein-Bézier Finite Elements of Arbitrary Order and Optimal Assembly Procedures. *SIAM Journal on Scientific Computing.* 33 (2011): 3087–3109.

[64] R. C. Kirby and K. T. Thinh. Fast simplicial quadrature–based finite element operators using Bernstein polynomials. *Numerische Mathematik.* 121(2) (2012): 261–279.

[65] W. J. Gordon and C. A. Hall. Construction of Curvilinear Coordinate Systems and Applications to Mesh Generation. *International Journal for Numerical Methods in Engineering.* 7 (1973): 461–77.

[66] W. J. Gordon and C. A. Hall. Transfinite Element Methods: Blending Function Interpolation over Arbitrary Curved Element Domains. *Numerische Mathematik.* 21 (1973): 109–129.

[67] B. Szabo and I. Babuška. Finite Element Analysis. *John Wiley & Sons, Inc,* 1991.

[68] F. Graff. Wave Motion in Elastic Solids. *Ohio State University, Ohio,* 1975.

[69] W. McLean. Strongly elliptic systems and boundary integral equations. *Cambridge University Press, Cambridge,* 2000.

[70] J. M. Melenk. On generalized finite-element methods. *PhD thesis, University of Maryland, College Park,* 1995.

[71] D. Gilbarg and N.S. Trudinger. Elliptic Partial Differential Equations of Second Order. *Springer–Verlag,* 1983.

[72] R. Leis. Boundary value problems in mathematical physics. *Teubner, Wiley,* 1989.

[73] P. Šolín, K. Segeth and I. Doležel. Higher-Order Finite Element Methods. *Chapman & Hall/CRC,* 2003.

[74] T. J. R. Hughes. The Finite Element Method: Linear Static and Dynamic Finite Element Analysis. *Englewood Cliffs, New Jersey: Prentice–Hall,* 1987.

[75] A. El Kacimi, O. Laghrouche, D. Ouazar, M. Shadi Mohamed, M. Seaid and J. Trevelyan. Enhanced Conformal Perfectly Matched Layers for Bernstein-Bézier Finite Element Modelling of Short Wave Scattering. *Computer Methods in Applied Mechanics and Engineering.* 355 (2019): 614–638.

[76] A. H. Stroud. Approximate Calculation of Multiple Integrals, *Prentice–Hall Series in Automatic Computation, Prentice–Hall, Englewood Cliffs, NJ,* 1971.

[77] T. Eibner and J. Melenk. Fast algorithms for setting up the stiffness matrix in *hp*-FEM: A comparison. *Computer Mathematics and Its Applications: Advances and Developments. (1994–2005), E. A. Lipitakis, ed., LEA Publishers, Athens, Greece.* (2006): 575–596.

[78] P. R. Amestoy, I. S. Duff and J. Y. L'Excellent. Multifrontal parallel distributed symmetric and unsymmetric solvers. *Computer Methods in Applied Mechanics and Engineering.* 184(2–4) (2000): 501–520.

[79] G. Karypis, V. Kumar. METISA Software Package for Partitioning Unstructured Graphs, Partitioning Meshes, and Computing Fill-Reducing Orderings of Sparse Matrices – *Version 4.0, University of Minnesota, 1998.*

[80] M. Arioli, J. Demmel and I.S. Duff. Solving sparse linear systems with sparse backward error. *SIAM Journal on Matrix Analysis and Applications.* 10(2) (1989): 165–190.

[81] Y. H. Pao and C. C. Mow. Diffraction of Elastic Waves and Dynamic Stress Concentrations. *Crane–Russak, New York,* 1973.